

Global simulations of axisymmetric radiative black hole accretion disks in general relativity with a sub-grid magnetic dynamo

Aleksander Sądowski^{1*}, Ramesh Narayan^{1*}, Alexander Tchekhovskoy^{2*}, David Abarca^{1*}, Yucong Zhu^{1*} and Jonathan C. McKinney^{3*}

¹ *Harvard-Smithsonian Center for Astrophysics, 60 Garden St., Cambridge, MA 02134, USA*

² *Lawrence Berkeley National Laboratory, 1 Cyclotron Rd, Berkeley, CA 94720, USA; Einstein Fellow*

³ *University of Maryland at College Park, Dept. of Physics, Joint Space-Science Institute, 1117 John S. Toll Building #082, College Park, MD 20742, USA*

24 September 2018

ABSTRACT

We present a sub-grid model that emulates the magnetic dynamo operating in magnetized accretion disks. We have implemented this model in the general relativistic radiation magnetohydrodynamic (GRRMHD) code KORAL, using results from local shearing sheet simulations of the magnetorotational instability to fix the parameters of the dynamo. With the inclusion of this dynamo, we are able to run 2D axisymmetric GRRMHD simulations of accretion disks for arbitrarily long times. The simulated disks exhibit sustained turbulence, with the poloidal and toroidal magnetic field components driven towards a state similar to that seen in 3D studies. Using this dynamo code, we present a set of long-duration global simulations of super-Eddington, optically-thick disks around non-spinning and spinning black holes. Super-Eddington disks around non-rotating black holes exhibit a surprisingly large efficiency, $\eta \approx 0.04$, independent of the accretion rate, where we measure efficiency in terms of the total energy output, both radiation and mechanical, flowing out to infinity. Super-Eddington disks around spinning black holes are even more efficient, and appear to extract black hole rotational energy through a process similar to the Blandford-Znajek mechanism. All the simulated models are characterized by highly super-Eddington radiative fluxes collimated along the rotation axis. We also present a set of simulations that were designed to have Eddington or slightly sub-Eddington accretion rates ($\dot{M} \lesssim 2\dot{M}_{\text{Edd}}$). None of these models reached a steady state. Instead, the disks collapsed as a result of runaway cooling, presumably because of a thermal instability.

Key words: accretion, accretion discs – black hole physics – relativistic processes – methods: numerical – galaxies: jets

1 INTRODUCTION

Black hole (BH) accretion disks are involved in some of the most energetic phenomena in the Universe - active galactic nuclei (AGN), microquasars, tidal disruptions of stars, γ -ray bursts. They power relativistic jets and provide feedback on the large-scale evolution of galaxies. Understanding the structure of accretion disks is therefore crucial for many applications in astrophysics.

Numerical simulations are a powerful tool for studying BH accretion disks, and can fill the gap between observational data (which are often limited because of the large distance to most ob-

jects), and theory (which is incapable of fully describing the non-linear turbulence in disks).

Gas can be accreted on BHs through hot or cold accretion flows (Yuan & Narayan 2014). The former are optically thin and predominantly radiatively inefficient because of long cooling timescales. The latter are optically thick, and may be either radiatively efficient (standard thin disks), or inefficient (slim disks) because of long radiative diffusion timescales. Optically thin flows have been extensively studied by means of general relativistic (GR) magnetohydrodynamical (MHD) simulations (e.g., De Villiers et al. 2003; Gammie et al. 2003; Anninos et al. 2005; Del Zanna et al. 2007; Narayan et al. 2012; McKinney et al. 2012; Tchekhovskoy & McKinney 2012). In optically thin flows, the radiation field is virtually decoupled from the gas, allowing for the radiation field to be neglected. On the other hand, simulating optically thick accre-

* E-mail: asadowski@cfa.harvard.edu (AS); rnarayan@cfa.harvard.edu (RN); atchekho@princeton.edu (AT); dabarca@cfa.harvard.edu (DA); yzhu@cfa.harvard.edu (YZ); jmck@umd.edu (JM);

tion is far more demanding since it requires coevolution of both the radiation and gas fields.

Numerical simulations of systems with radiation is a non-trivial problem; Solving the radiation transport equations is often overwhelmingly expensive, so various approximations are needed. The most common approach in the past was to invoke flux limited diffusion (FLD) (e.g., Hirose et al. 2009b; Blaes et al. 2011; Ohsuga et al. 2009; Ohsuga & Mineshige 2011), which assumes that the radiative flux follows the gradient of the radiative energy density. Its Achilles heel is that it does not satisfy momentum conservation (since FLD does not keep track of the radiation pressure) and also does not work properly in the optically thin limit.

As an alternative to FLD, the M1 radiative closure (Levermore 1984; Dubroca & Feugeas 1999) has recently been adopted by a number of groups (Sądowski et al. 2013a; Skinner & Ostriker 2013; McKinney et al. 2013) as a more accurate treatment of the radiation field. The advantage of M1 is that it addresses the two fundamental problems of FLD (momentum conservation and optically thin limit) while also working in a general relativistic (GR) framework. However, M1 has its own limitations – it cannot handle photon distributions with complex angular structure. Jiang et al. (2012) have overcome the latter limitation by estimating the radiative stress energy tensor through a short-characteristics solver that makes use of a large number of angles. They have applied the code to shearing sheet local simulations (Jiang, Stone, & Davis 2013). Very recently, Jiang, Stone, & Davis (2014) have switched to an even more self-consistent approach where specific intensities at fixed angles are evolved directly, and the radiative stress energy tensor is constructed on the go from the exact intensity distribution.

Although many numerical codes are available for evolving black hole accretion disks with gas and radiation (see above), even the simplest problems are still prohibitively expensive to simulate in full 3D. One saving grace is the case of very large accretion rates (i.e. exceeding the Eddington accretion rate¹). Highly accreting systems are feasible to simulate in three dimensions (McKinney et al. 2013) because their short viscous timescales and large geometrical thickness allows for relatively short duration of simulations and low resolution, respectively. Simulating disks at lower accretion rates is much more demanding and may be beyond reach for the near future.

Obviously, axisymmetric, two-dimensional (2D) simulations are computationally much less expensive than three-dimensional (3D), so one can simulate a wider range of systems in 2D. What has prevented such simulations in the past is the anti-dynamo theorem (Cowling 1933), which states that axisymmetric ideal MHD systems do not have any dynamo mechanism to regenerate the magnetic field. This means 2D axisymmetric simulations cannot regenerate their magnetic fields and therefore accretion will die after a short time — i.e. the poloidal magnetic field quickly decays and

¹ In this work we adopt the following definition for the Eddington accretion rate,

$$\dot{M}_{\text{Edd}} = \frac{L_{\text{Edd}}}{\eta_0 c^2}, \quad (1)$$

where $L_{\text{Edd}} = 1.25M/M_{\odot} \times 10^{38}$ ergs/s is the Eddington luminosity, and η_0 is the radiative efficiency of a thin disk for a given spin a_* ,

$$\eta_0 = 1 - \sqrt{1 - \frac{2}{3R_{\text{ISCO}}}}, \quad (2)$$

and R_{ISCO} is the radius of the Innermost Stable Circular Orbit (ISCO). According to this definition, any thin, radiatively efficient disk accreting at \dot{M}_{Edd} has luminosity L_{Edd} .

it is not replaced because of this lack of dynamo. To get over this problem, we introduce here a sub-grid dynamo model which emulates the missing dynamo process, and drives the properties of turbulence towards a state characteristic of disk MRI turbulence in local 3D simulations. We apply our method to radiative accretion flows and simulate a number of disks models covering a wide range of accretion rates.

The paper is organized as follows. In Section 2 we briefly introduce the numerical methods we use, with details given in Appendices A and B. In Section 3 we present the global simulations we performed. Finally, in Section 4 we summarize our work.

2 NUMERICAL METHODS

2.1 GRRMHD code — KORAL

We use the general relativistic radiation magnetohydrodynamics (GRRMHD) code KORAL (Sądowski et al. 2013a, 2014), which employs a Godunov scheme to evolve the rest mass, energy and momentum conservation equations in a fixed, arbitrary spacetime using finite-difference methods. The magnetic field is evolved according to the induction equation and the divergence-free criterion is enforced using the flux-constrained Tóth (2000) scheme as described in Gammie et al. (2003). KORAL simultaneously evolves two fluids, magnetized gas and radiation, which exchange energy and momentum via mutual interactions.

The conservation laws are described by the following general set of equations,

$$(\rho u^\mu)_{;\mu} = 0, \quad (3)$$

$$(T_v^\mu)_{;\mu} = G_v, \quad (4)$$

$$(R_v^\mu)_{;\mu} = -G_v, \quad (5)$$

where ρ is the gas density in the comoving fluid frame, u^μ is the gas four-velocity as measured in the “lab frame”, and T_v^μ is the MHD stress-energy tensor in this frame,

$$T_v^\mu = (\rho + u_g + p_g + b^2)u^\mu u_\nu + (p_g + \frac{1}{2}b^2)\delta_v^\mu - b^\mu b_\nu, \quad (6)$$

R_v^μ is the stress-energy tensor of radiation, and G_v is the radiative four-force describing the interaction between gas and radiation (both are described in detail in Section 2.2). Here u_g and $p_g = (\Gamma - 1)u_g$ represent the internal energy and pressure of the gas in the comoving frame and b^μ is the magnetic field 4-vector (Gammie et al. 2003). The magnetic pressure is $p_{\text{mag}} = b^2/2$.

In the coordinate basis Eqs. (3)-(5) take the form,

$$\partial_i(\sqrt{-g}\rho u^i) + \partial_i(\sqrt{-g}\rho u^i) = 0, \quad (7)$$

$$\partial_i(\sqrt{-g}T_v^i) + \partial_i(\sqrt{-g}T_v^i) = \sqrt{-g}T_\lambda^k \Gamma_{\nu k}^\lambda + \sqrt{-g}G_\nu, \quad (8)$$

$$\partial_i(\sqrt{-g}R_v^i) + \partial_i(\sqrt{-g}R_v^i) = \sqrt{-g}R_\lambda^k \Gamma_{\nu k}^\lambda - \sqrt{-g}G_\nu, \quad (9)$$

where $\sqrt{-g}$ is the metric determinant, and $\Gamma_{\nu k}^\lambda$ are Christoffel symbols.

KORAL adopts the ideal MHD approximation and assumes that the electric field vanishes in the fluid rest frame. The induction equation then takes the following form in coordinate basis,

$$\partial_i(\sqrt{-g}B^i) = -\partial_j(\sqrt{-g}(b^j u^i - b^i u^j)), \quad (10)$$

where B^i is the magnetic field three-vector (Komissarov 1999) which satisfies,

$$b^i = B^i u^\mu g_{i\mu}, \quad (11)$$

$$b^i = \frac{B^i + b^i u^i}{u^i}. \quad (12)$$

The flux-interpolated constrained transport (Flux-CT) method of Tóth (2000) prevents numerical generation of spurious magnetic monopoles. For the gas and magnetic fields, we use standard numerical methods as described in previous papers (Gammie et al. 2003; McKinney 2006; McKinney et al. 2012; Sądowski et al. 2013a, 2014).

2.2 Radiative closure

At each time step, radiative energy density (R^t) and radiative fluxes (R^i) are evolved following Eq. (9). To calculate the time derivatives we need to know all the remaining components of radiation stress-energy tensor $R^{\mu\nu}$. For this purpose we make use of the M1 closure scheme (Levermore 1984). In this approach, we assume that the radiation tensor is isotropic and satisfies Eddington closure, not in the fluid frame, but in the orthonormal “rest frame” of the radiation. The latter is defined as the frame in which the radiative flux vanishes.

A covariant formulation of the M1 scheme was introduced in Sądowski et al. (2013a) which we have adopted. Herein, we give only the essential formulae and ask the reader to refer to that paper for details.

Knowing $R^{\mu\nu}$ we calculate the time-component of the radiative rest-frame four velocity, u_R^t , and the radiative energy density in this frame, E_R , by solving the following two equations,

$$g_{\mu\nu} R^{\mu\nu} = -\frac{8}{9} E_R^2 (u_R^t)^2 + \frac{1}{9} E_R^2 g^{tt}, \quad (13)$$

$$R^t = \frac{4}{3} E_R (u_R^t)^2 + \frac{1}{3} E_R g^{tt}. \quad (14)$$

These quantities are then used to find the spatial components of u_R^{μ} using the time component of,

$$R^{\mu\nu} = \frac{4}{3} E_R u_R^{\mu} u_R^{\nu} + \frac{1}{3} E_R g^{\mu\nu}. \quad (15)$$

Once we have u_R^{μ} and E_R , we use the remaining components of Eq. (15) to compute full radiative stress energy tensor $R^{\mu\nu}$.

M1 closure is superior to the Eddington closure and FLD, especially for optically thin media. It is a simple and elegant closure scheme which evolves both the radiation energy density and radiation fluxes. However, M1 allows for only a very limited set of the specific intensity distributions (boosted isotropic), and therefore is far from perfect. More advanced radiation transfer schemes have been developed (e.g., Jiang et al. 2012; Jiang, Stone, & Davis 2014). The main advantage of M1 closure over these more advanced schemes is that it is covariant, fast, and local; also, it has been implemented in radiation GRMHD codes whereas none of the other schemes have yet been attempted with general relativity. In our view, it is reasonable to assume that M1 catches most of the relevant dynamics of radiative BH accretion flows.

2.3 Radiative four-force

The four-vector G^{μ} describes the interaction between gas and radiation. Sądowski et al. (2014) introduced covariant formalism for computing the interaction due to absorption and elastic scattering.

In this paper, we account also for energy exchange via Comptonization, which we implement in a similar way to that described in Kawashima et al. (2009). Detailed derivation is given below in Section 2.4.

We write the four-force G^{μ} as

$$G^{\mu} = G_0^{\mu} + G_{\text{Compt}}^{\mu}, \quad (16)$$

where G_{Compt}^{μ} describes the effect of Comptonization, and G_0^{μ} corresponds to absorption and Thomson scattering and is given by (Sądowski et al. 2014),

$$G_0^{\mu} = -\rho(\kappa_a + \kappa_{\text{es}}) R^{\mu\nu} u_{\nu} - \rho(\kappa_{\text{es}} R^{\alpha\beta} u_{\alpha} u_{\beta} + \kappa_a 4\pi B) u^{\mu}, \quad (17)$$

where κ_a and κ_{es} are absorption and scattering opacities, respectively, and $B = aT_g^4/4\pi$ (a is the radiation constant) is the intensity of black body radiation for gas with temperature T_g .

The source term associated with the radiative four-force is stiff whenever the gas is optically thick. KORAL deals with this problem by applying it semi-implicitly. That is, at each cell center, after applying the advective operator (the spatial gradient terms in equations 7-9), the following set of equations is solved,

$$T_{v,(n+1)}^t - T_{v,(n)}^t = \Delta t G_{v,(n+1)}^t, \quad (18)$$

$$R_{v,(n+1)}^i - R_{v,(n)}^i = -\Delta t G_{v,(n+1)}^i, \quad (19)$$

where the subscripts (n) and ($n+1$) denote values at the beginning and end of a time step of length Δt , respectively. For details of this procedure, see Sądowski et al. (2014).

2.4 Thermal Comptonization

In the absence of Comptonization, in fluid frame orthonormal coordinates the time and spatial components of the radiative four-force (Eq. 17) take the form,

$$\widehat{G}^0 = \kappa_a \rho (\widehat{E} - 4\pi \widehat{B}), \quad (20)$$

$$\widehat{G}^i = (\kappa_a + \kappa_{\text{es}}) \rho \widehat{F}^i, \quad (21)$$

where

$$4\pi \widehat{B} = aT_g^4, \quad (22)$$

and T_g is the temperature of the gas. Equation (20) describes the rate of change of the fluid energy density as a result of energy gain through absorption, $\kappa_a \rho \widehat{E}$, and energy loss through emission, $\kappa_a \rho (4\pi \widehat{B})$. For simplicity, we treat radiation as a blackbody, hence we define an effective radiation temperature T_r in the fluid frame via

$$\widehat{E} = aT_r^4. \quad (23)$$

Thus, equation (20) shows that gas gains energy at a rate proportional to T_r^4 and loses energy proportional to T_g^4 . As a result, the two temperatures are pushed towards each other, i.e., the system is driven towards thermal equilibrium. Note that κ_{es} does not appear in the energy equation. This is because Thomson scattering redirects photons, but it does not transfer energy.

Equation (21) describes the rate of change of the fluid momentum density. The gas acquires the momentum of each photon that it either absorbs or scatters. Since the re-emission of radiation is symmetric in the fluid frame, there is no counter-balancing term with a negative sign. Note that the fluid gains momentum density in a direction parallel to the radiation flux \widehat{F}^i , and the radiation loses a corresponding amount of momentum density. Hence the system

is driven towards a state in which there is no relative motion between the fluid and radiation frames, i.e., no radiation flux in the fluid frame ($u^\mu = u_R^\mu$).

The main effect of Comptonization is that scattering causes not just momentum transfer between the radiation and gas, but also energy transfer. A soft photon of energy ϵ_0 which scatters off a thermal electron with temperature T_e on average gains an energy $\langle \Delta\epsilon \rangle$ given by the following two expressions in the non-relativistic and ultra-relativistic limits:

$$\langle \Delta\epsilon \rangle = \left(\frac{4kT_e}{m_e c^2} \right) \epsilon_0, \quad 4kT_e \ll m_e c^2, \quad (24)$$

$$\langle \Delta\epsilon \rangle = \left(\frac{4kT_e}{m_e c^2} \right)^2 \epsilon_0, \quad 4kT_e \gg m_e c^2. \quad (25)$$

For a general temperature, using the result given in equation (2.43) in Pozdnyakov et al. (1983), we have obtained a good fitting function (maximum fractional error 1.2%) which works for all T_e

$$\langle \Delta\epsilon \rangle = \epsilon_0 \left(\frac{4kT_e}{m_e c^2} \right) \left[1 + 3.683 \left(\frac{kT_e}{m_e c^2} \right) + 4 \left(\frac{kT_e}{m_e c^2} \right)^2 \right] \left[1 + \left(\frac{kT_e}{m_e c^2} \right) \right]^{-1}. \quad (26)$$

The above expressions are valid so long as the photon is soft, i.e., the radiation temperature is much less than the gas temperature. When the two temperatures are equal, thermodynamics guarantees that there is no energy transfer between gas and radiation. Similarly, when the radiation temperature is larger than the gas temperature, we expect energy to flow from the radiation to the gas. To allow for these effects, we modify equation (20) by introducing an extra contribution to \widehat{G}^0 ,

$$\begin{aligned} \widehat{G}_{\text{Compt}}^0 &= -\kappa_{\text{es}} \rho \widehat{E} \left[\frac{4k(T_g - T_r)}{m_e c^2} \right] \times \\ &\times \left[1 + 3.683 \left(\frac{kT_e}{m_e c^2} \right) + 4 \left(\frac{kT_e}{m_e c^2} \right)^2 \right] \left[1 + \left(\frac{kT_e}{m_e c^2} \right) \right]^{-1}, \end{aligned} \quad (27)$$

where we have replaced T_e by T_g . The negative sign in the Compton term is because gas cools when $T_g > T_r$. The cooling is proportional to the radiation energy density, \widehat{E} , and to the number of scatterings per unit time, $\kappa_{\text{es}} \rho$. Except for the two final factors in square parentheses, which are an approximate correction for relativistic temperatures, equation (27) is identical to the prescription used by Kawashima et al. (2009).

As far as the momentum equation is concerned, we assume that the Compton-scattered radiation is symmetric in the fluid frame and carries no net momentum (a fairly good approximation in the soft photon limit). Under this approximation, we do not modify equation (21).

Eq. (27) gives the fluid-frame energy transfer rate due to Comptonization. To obtain the corresponding ‘‘lab frame’’ four-vector G_{Compt}^μ (Eq. 16) we write,

$$G_{\text{Compt}}^\mu = \widehat{G}_{\text{Compt}}^0 u^\mu. \quad (28)$$

We have included the above version of Comptonization in the simulations described in this paper. That is, we solve equations (4) and (5) using equations (27) and (21), where \vec{B} is given by equation (22) and T_r is given by equation (23). Note that this is an extremely simple prescription. The main weakness of this approach is that it does not conserve photon number during scattering. Instead it assumes perfect blackbody and uses equation (23) to obtain the radiation temperature, thus missing any effects associated with spectral hardening and a dilute blackbody.

2.5 Sub-grid dynamo

Magnetic stresses generated via MRI turbulence are responsible for angular momentum transport and energy dissipation in BH accretion disks. The same turbulence also dissipates magnetic field. The field is, however, regenerated through a dynamo (e.g., Parker 1955; Brandenburg et al. 1995). The balance of these two processes leads to a saturated quasi-equilibrium state.

Evolution of magnetic fields has been studied extensively by means of local shearing box simulations (e.g., Turner et al. 2003; Krolik et al. 2007; Blaes et al. 2007; Blackman, Penna, & Varnière 2008; Guan et al. 2009), as well as global simulations (Sorathia et al. 2012). It has been shown that for the Keplerian shear the magnetic field saturates at a turbulent state characterized by a mean magnetic field angle,

$$\xi = \frac{\hat{b}' \hat{b}^\varphi}{b^2} \approx 0.25, \quad (29)$$

and at magnetic to total pressure ratio,

$$\beta' = \frac{P_{\text{mag}}}{P_{\text{tot}}} \approx 0.1. \quad (30)$$

Reaching the saturated quasi-stationary state is possible only in 3D simulations. If only axisymmetry is assumed, the anti-dynamo theorem (Cowling 1933) implies that the magnetic field cannot be maintained by dynamo action. Axisymmetric MHD simulations of accretion disks are therefore not very useful. Not only is their duration limited (decaying poloidal magnetic field implies decaying turbulence), but even at early times in these simulations the configuration of magnetic field is far from that expected in the saturated state of 3D MRI turbulence. Typically, an axisymmetric simulation may last up to $\sim 5000 GM/c^2$, i.e., 5 orbits at radius $R = 20$.

The evolution of the mean magnetic field may be described under the mean field theory by the following equation (Brandenburg 2001),

$$\frac{\partial}{\partial t} \vec{B} = \alpha \nabla \times \vec{B} + \eta \nabla^2 \vec{B}, \quad (31)$$

where α and η , are the dynamo, and magnetic diffusivity coefficients, respectively. The first term on the right hand side describes the dynamo effect which generates magnetic field, and the second corresponds to the dissipation of magnetic field.

Direct implementation of the mean field equation into axisymmetric models is possible in resistive, non-ideal GRMHD codes (Bucciantini & Del Zanna 2013). However, such dynamo closure is not unique, and one still has to arbitrarily (basing on three dimensional studies) specify values of α and η .

In this paper we present a simpler method, which could be used in non-resistive, ideal MHD codes, i.e., codes which assume that the electric field disappears in the gas comoving frame. We use Eq. 31 and the expected properties of the magnetic field in the saturated state (Eqs. 29 - 30), and construct a sub-grid dynamo model which injects a weak poloidal magnetic field into the simulation on top of the preexisting magnetic field, and drives the total field towards the prescribed characteristics consistent with the saturated state. A detailed derivation is given in Appendix A. Below we give only the ultimate formulae implemented in KORAL.

At each time step, an estimate of the dynamo-generated magnetic field is superimposed on the existing magnetic field. The change in the poloidal magnetic field is calculated through the toroidal vector potential,

$$dA_\varphi = -\alpha_{\text{dyn}} \Omega_K R g_{\varphi\varphi} B^\varphi f_R f_\theta f_\xi f_{\text{eq}} dt, \quad (32)$$

where α_{dyn} is an arbitrary coefficient, dt is the time step, $\Omega_K = R^{-3/2}$, θ is the polar coordinate, B^φ is the toroidal component of the magnetic three-vector (Eqs. 11-12), f_R , f_θ and f_ξ are arbitrary factors damping the dynamo process in the plunging region, outside the disk, and in regions with too large magnetic field angle ξ , respectively, and f_{eq} makes the dynamo flip sign across the equatorial plane. The dynamo-generated vector potential dA_φ is then converted into poloidal magnetic field through $d\vec{B} = \nabla \times d\vec{A}$, which is then superimposed on top of the existing magnetic field.

Shear constantly generates azimuthal magnetic field from radial field. In three dimensions, the field strength saturates because of dissipation. We mimic this saturation by damping the azimuthal component of the lab-frame magnetic field in regions where magnetic pressure exceeds the prescribed pressure ratio β' . We do it on the orbital timescale according to,

$$dB^\varphi = -\alpha_{\text{damp}} \Omega_K B^\varphi f_R f_\theta f_{\beta'} dt, \quad (33)$$

where $\alpha_{\text{damp}} = 1.0$, and $f_{\beta'}$ is a factor which switches off the damping in regions of too low pressure ratio β' . Because of axisymmetry, changing B^φ does not violate the divergence-free condition. Detailed formulae are given in Appendix A.

The sub-grid dynamo model is applied at every time substep, after all the other operators have been accounted for. First, the vector potential dA_φ (Eq. 32) is converted to poloidal magnetic dB_{dyn}^p , and is added to the existing field B^p . Secondly, the azimuthal magnetic field is damped according to Eq. 33. The total MHD stress-energy tensor components T_i^j (the conserved quantities, Eq. 6) are left unchanged during both steps. Thus, any change in the magnetic energy density causes a compensating change in the gas internal energy.

2.6 Radiative viscosity

In this work, we slightly modify the radiative flux terms in Eq. 9 by introducing a radiative viscosity which is effective only in the optically thin region and which helps to avoid artificial centrifugal shocks, which are known to occur near the polar axis with M1 closure (Sądowski et al. 2013a). We replace the original, M1-based flux term, $R_{v,\text{M1}}^i$, with,

$$R_v^i = R_{v,\text{M1}}^i + R_{v,\text{visc}}^i, \quad (34)$$

where $R_{v,\text{visc}}^i = -2\nu E_R \sigma_v^i$ is the viscous correction to the radiative stress-energy tensor, which depends on the photon mean-free path, radiative energy density in the radiation rest frame, E_R , and the shear tensor, σ_v^i , estimated from the velocities of the radiative rest frames of the given cell and its neighbours.

Detailed formulae, and tests are given in Appendix B.

3 GLOBAL SIMULATIONS

3.1 Numerical setup

All the simulations were performed in 2.5 dimensions, i.e., we assumed axisymmetry, but we allowed for non-zero φ -components of vectors (e.g., angular velocity and azimuthal radiative flux). We used Kerr-Schild horizon-penetrating coordinates. The internal grid (x_1, x_2) was uniform and was related to the Kerr-Schild radial and polar coordinates (R, θ) by,

$$R = R_0 + e^{x_1}, \quad (35)$$

$$\theta = \left(\frac{\tan(H_0\pi(x_2 - 0.5))}{\tan(H_0\pi/2)} + 1 \right) \frac{\pi}{2}. \quad (36)$$

As a result, the grid points were spaced roughly logarithmically in radius, and concentrated towards the equatorial plane, with the density of the points there depending on H_0 . The internal radial coordinate x_1 was chosen to correspond to the range of radii between R_{min} and R_{max} , while x_2 covered range $(\epsilon, 1 - \epsilon)$, with $\epsilon = 0.005$. Values of R_{min} , R_{max} , R_0 , and H_0 , for each simulation are given in Table 1.

At the inner radial boundary (located at least five cells under the BH horizon) we applied an outflow boundary condition by copying values of all the primitive quantities to the ghost cells. At the outer radial boundary we adopted a similar approach, except that we prevented the inflow of gas or radiation by resetting negative radial velocities to zero. The polar axis was treated with reflective boundary condition. To ensure stability in this region the primitive quantities in the two closest cells to the polar axis were appropriately overwritten with the values from the third cell (McKinney et al. 2012). Scalars, radial and azimuthal components of vectors were copied, and the polar components were interpolated towards zero to satisfy this reflective boundary condition. As described in Sądowski et al. (2013a), we evolved entropy as an auxiliary quantity which was used when the regular, energy-based, inversion failed.

We adopted the sub-grid dynamo prescription (Section 2.5 and Appendix A) which mimics the three-dimensional evolution of magnetic fields. For all the runs we adopted $\alpha_{\text{dyn}} = 0.05$, $\alpha_{\text{damp}} = 1.0$, $\xi_{\text{dyn}} = 0.25$, and $\beta'_{\text{damp}} = 0.1$. We also included the radiative viscosity (Appendix B) with $\alpha_{\text{rad}} = 0.1$.

3.2 Initial state

All the simulations were started from an equilibrium torus rotating around a $10M_\odot$ BH, which was threaded by initial, poloidal seed magnetic field.

The gas was initially set as a hydrodynamical equilibrium torus following Penna et al. (2013a). Its angular velocity at the equatorial plane was set to a constant fraction of $\xi = 0.708$ of the Keplerian angular velocity outside radius $R_1 = 42$, and followed fixed angular momentum inside that radius. The angular momentum was kept constant along the von-Zeipel cylinders. The inner edge of the torii was chosen at $R_{\text{in}} = 22$. The density was fixed by setting the entropy constant \mathcal{K} to the values given in Table 1, and by assuming $\Gamma = 5/3$. This setup results in an equilibrium torus that has a vertical surface density profile that is nearly constant with radius. A radius independent density profile was desired since it helps keep the accretion rate constant with time. On the other hand, the radial extent of the torus was limited only to $R \lesssim 400$, and this fact could limit the available range of the inflow equilibrium.

So far, we have specified a torus in pure hydrodynamical equilibrium. To introduce the initial radiation field, we decided to start simulations from the local thermal equilibrium (LTE) by solving for gas (and radiation) equilibrium temperature T , using,

$$p_{\text{tot}} = p_{\text{gas}} + p_{\text{rad}} = k_B \rho T + \frac{4}{3} \sigma T^4, \quad (37)$$

where p_{tot} is the total pressure given by the hydrodynamical torus solution, and p_{gas} and p_{rad} are gas and radiation pressures of the LTE torus, respectively. Because of the inconsistency in the values of Γ of the initial hydrodynamical torus ($\Gamma = 5/3$), and the resulting effective Γ of the gas and radiation mixture ($\Gamma \approx 4/3$ for radiation pressure dominated medium), the torus is not in the perfect equilibrium at early times. However, it remains in a relatively steady state

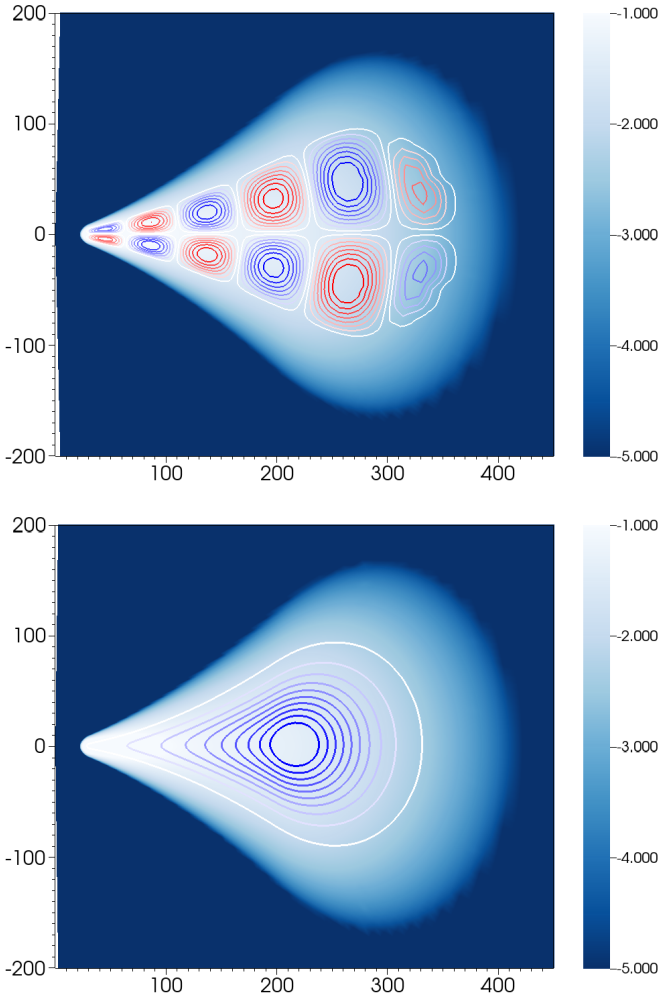


Figure 1. Snapshots of logarithm of density for the initial equilibrium torii for runs 302a0 and 302a9mad. Contours follow the lines of the initial poloidal magnetic field. Red and blue correspond to clock- and counter-clockwise loops, respectively.

until the magnetorotational instability (MRI) grows, after which the initial state is forgotten.

The initial magnetic field threading the torus was purely poloidal and consisted of either a single or multiple loops. Multiple loops were constructed from the vector potential following Penna et al. (2013a). In their notation we adopted $r_{\text{start}} = 27.5$, $r_{\text{end}} = 350$ and $\lambda = 2.5$. To make the loops flip polarity across the equatorial plane we additionally multiplied the vector potential by $\sin(\pi/2 - \theta)$. The single loop, on the contrary, was set up according to the vector potential given by,

$$A_\varphi = \max\left(\left(\frac{\rho R^2}{6 \times 10^{-5} \text{g/cm}^3 G^2 M^2 / c^4}\right)^2 - 0.02, 0\right) (\sin \theta)^4. \quad (38)$$

The initial torus for the two configurations of the magnetic field is shown in Fig. 1.

3.3 Super-critical disks around non-rotating BHs

We performed a set of eight simulations with multiple loops of the initial magnetic field and a non-rotating BH. The initial torus in all simulations was the same (but for the seed magnetic field), but we

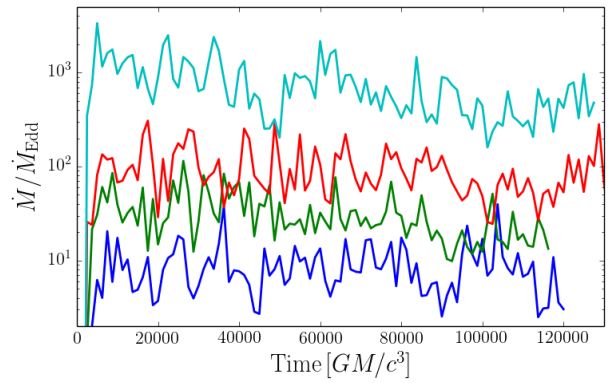


Figure 2. Time profiles of the accretion rate through the BH horizon for models (top to bottom) r302a0, r301a0, r3015a0, and r300a0.

varied the entropy parameter \mathcal{K} responsible for scaling the density. The four simulations with the highest densities (models r302a0 – r300a0, see Table 1) evolved into a quasi-stationary states corresponding to accretion rates $\dot{M}/\dot{M}_{\text{Edd}} = 10 \div 560$. The other four did not provide equilibrium solutions, and collapsed (model r299a0 only after $t \approx 70,000$). They are discussed in Section 3.5. Below we describe in detail the disks which reached equilibrium. The discussion is extended to spinning BHs in Section 3.4.

3.3.1 General properties

Figure 2 shows the accretion rate history for the four equilibrium runs. The different accretion rates are mostly due to the different starting densities of the initial torus. Another (less important) factor that affects the accretion rate is the resulting radial velocity. In the standard disk picture, optical depth of the disk (which depends on the initial torus density) determines how radiatively efficient it is, and also affects (although slightly in our cases) the radial velocity.

For all four simulations the accretion rate remains roughly constant or slightly decreases with time. This proves that the sub-grid dynamo is effective in keeping the turbulence and accretion alive. The weak decreasing trend in accretion rate results both from the depletion of initial gas reservoir, and increasing magnetic pressure near the BH.

The history of the magnetic flux accumulated on the BH horizon, parametrized through,

$$\varphi = \frac{1}{\sqrt{\langle \dot{M} \rangle}} \frac{4\pi}{2} \int_0^\pi \int_0^{2\pi} \sqrt{-g} |B'| d\varphi d\theta, \quad (39)$$

where $\langle \dot{M} \rangle$ is the average accretion rate for each run, is shown in Figure 3. All four runs were initiated with quadrupole magnetic field, so magnetic field with alternating polarity is expected to reach BH with time. This results in roughly chaotic evolution of the magnetic flux parameter. The average value of φ over entire duration of simulations falls between $\varphi = 14.4$ for r300a0, and $\varphi = 23.5$ for r302a0, and is significantly below the Magnetically Arrested Disk (MAD) critical value $\varphi_{\text{MAD}} \approx 50$ (Tchekhovskoy et al. 2010; Tchekhovskoy & McKinney 2012).

Figure 4 shows snapshots from three models, r299a0 (before collapse, see Section 3.5), r300a0, and r301a0. Colors show the logarithm of density. Solid and dashed lines show the scale-height,

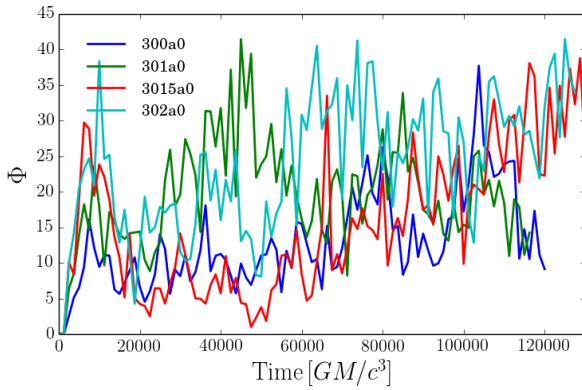
Table 1. Model parameters

Name	a_*	B field	\mathcal{K}	β_{\max}	resolution ($N_R \times N_\theta$)	grid ($R_{\min} / R_{\max} / R_0 / H_0$)	t_{\max}	$\langle \dot{M} \rangle / \dot{M}_{\text{Edd}}$
super-critical disks, non-rotating BH:								
r302a0	0.0	multi.	100	10	(264 x 200)	(1.85 / 5000 / 1.0 / 0.6)	128,000	559
r3015a0	0.0	multi.	200	10	(264 x 200)	(1.85 / 5000 / 1.0 / 0.6)	151,000	73.1
r301a0	0.0	multi.	300	10	(264 x 224)	(1.85 / 5000 / 1.0 / 0.6)	111,000	24.3
r300a0	0.0	multi.	500	10	(264 x 240)	(1.85 / 5000 / 1.0 / 0.6)	111,000	9.6
super-critical, rotating BH:								
r302a9madhb	0.9	single	100	10	(240 x 240)	(1.3 / 5000 / 1.0 / 0.4)	90,500	3050
r302a9mad	0.9	single	100	50	(240 x 240)	(1.3 / 5000 / 1.0 / 0.4)	90,500	2060
r300a9	0.9	multi.	500	10	(264 x 240)	(1.3 / 5000 / 1.0 / 0.6)	54,000	11.9
thin, collapsing disks:								
r299a0	0.0	multi.	800	10	(264 x 216)	(1.85 / 5000 / 1.0 / 0.7)	155,000	2.1*
r297v3a0	0.0	multi.	1000	10	(288 x 300)	(1.85 / 1000 / 1.0 / 0.85)	25,050	N/A
r297v2a0	0.0	multi.	1050	10	(288 x 312)	(1.9 / 1000 / 1.25 / 0.9)	27,000	N/A
r297v1a0	0.0	multi.	1100	10	(288 x 300)	(1.9 / 1000 / 1.25 / 0.9)	24,100	N/A
r298a9	0.9	multi.	1000	10	(280 x 300)	(1.3 / 5000 / 1. / 0.85)	33,700	N/A

multi. - multiple magnetic field loops; single - single magnetic loop;

β_{\max} - maximal value of magnetic $\beta = p_{\text{tot}}/p_{\text{mag}}$; t_{\max} - duration of simulation.

* Before $t = 70,000$.


Figure 3. Evolution of the magnetic flux parameter φ (Eq. 39) with time.

$$\theta_H = \sqrt{\frac{2\pi}{\Sigma} \int_0^\pi \rho |\theta - \pi/2|^2 \sqrt{g_{\theta\theta}} d\theta}, \quad (40)$$

where

$$\Sigma = 2\pi \int_0^{2\pi} \rho \sqrt{g_{\theta\theta}} d\theta, \quad (41)$$

is the surface density, and the location of the photosphere² respectively. The turbulent structure of each disk is clear. Increasing accretion rate results both in larger densities, and thicker (in terms of the scale-height and the photosphere location) disks.

3.3.2 Resolving MRI

To verify that the adopted resolution is enough to resolve the fastest growing mode of the MRI we calculate the vertically averaged pa-

² Plots show the photosphere surface obtained by integrating the optical depth from the polar axis to $\tau = 1$ along a fixed radius, while in Section 3.3.7, we perform the integrals from the outer boundary towards the BH along a constant polar angle.

rameter Q^θ (Hawley et al. 2011),

$$Q^\theta = \frac{2\pi}{\Sigma} \int_0^\pi \rho \frac{2\pi}{\Omega \Delta x^\theta} \frac{|B^\theta|}{\sqrt{\rho}} \sqrt{g_{\theta\theta}} d\theta, \quad (42)$$

where Δx^θ is the grid cell size in θ , and Ω is the angular velocity. Figure 5 shows profiles of the MRI resolution parameter for all the runs with non-spinning BHs obtained by averaging values calculated for each snapshot (taken every $\Delta t = 50$). For all radii $R \lesssim 60$, Q^θ significantly exceeds 10 making MRI reasonably resolved (Hawley et al. 2013).

3.3.3 Rest mass fluxes

Figure 6 shows the averaged profiles of the total (solid), inflowing (dashed), and outflowing (dotted lines) accretion rate. The total accretion rate for all four runs is roughly constant between the BH horizon and radius $R_{\text{eq}} \approx 60$, which limits the range of the inflow-outflow equilibrium. The inflowing accretion rate departs from the net accretion rate outside radius $R_{\text{out}} \approx 20$, where gas starts to flow out in the wind region (dotted lines). The wind mass loss rates equal the accretion rates near radius $R \approx 40$ for all four runs. The radial slope of the inflowing accretion rate outside R_{eq} is close to $\dot{M}_{\text{in}} \propto R^1$, but is rather poorly constrained because of the limited range of the equilibrium solution.

Narayan et al. (2012) and Sądowski et al. (2013b) discussed properties of the rest mass flux in three-dimensional simulations of radiatively inefficient, optically thin accretion disks. For their simulations with a non-rotating BH, no significant mass outflow was present inside $R \approx 50$ (compared to our $R \approx 20$). Similar conclusions may be drawn from comparing simulations with spinning BHs (Fig. 15). These facts suggest that optically thick, radiation pressure dominated disks produce winds more effectively than optically thin disks.

3.3.4 Energy fluxes

Figure 7 shows the averaged profiles of the energy fluxes normalized by the rest mass accretion rate at the horizon, and integrated over the full solid angle, for a representative run r300a0. The solid

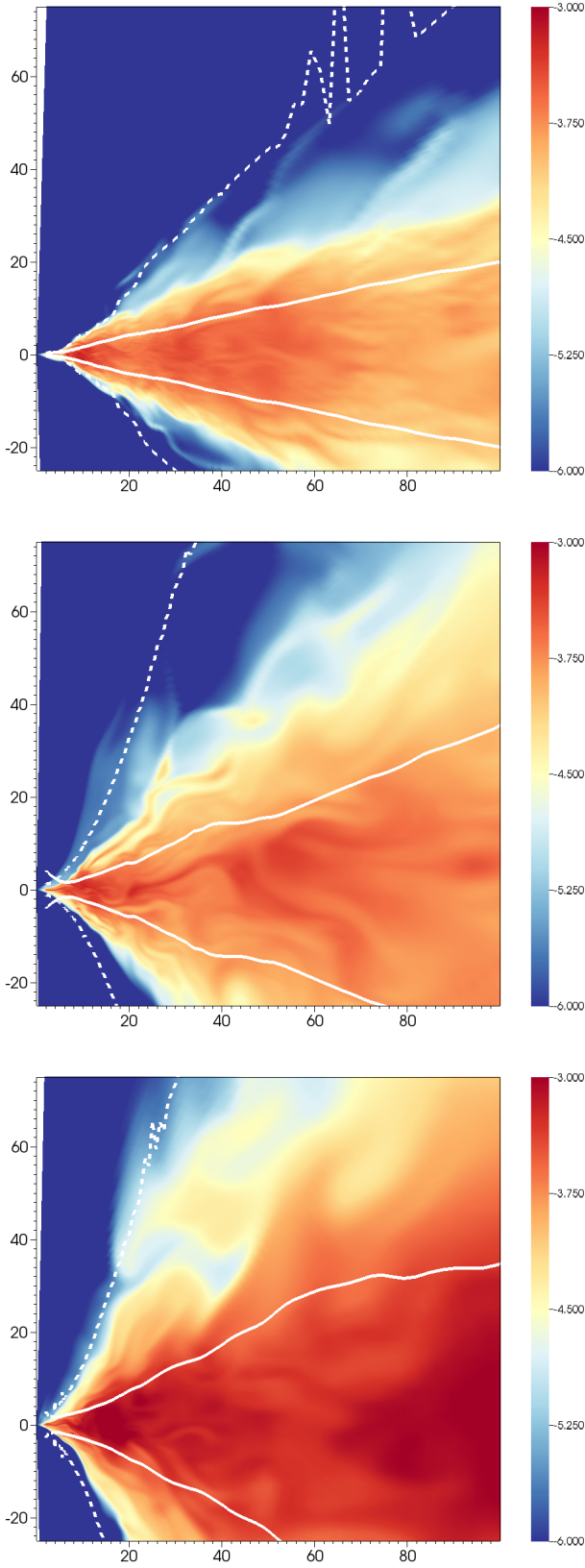


Figure 4. Snapshots of logarithm of density for models r299a0, r300a0, and r301a0 (top to bottom). Solid and dashed lines show locations of the density scale height and the photosphere, respectively.

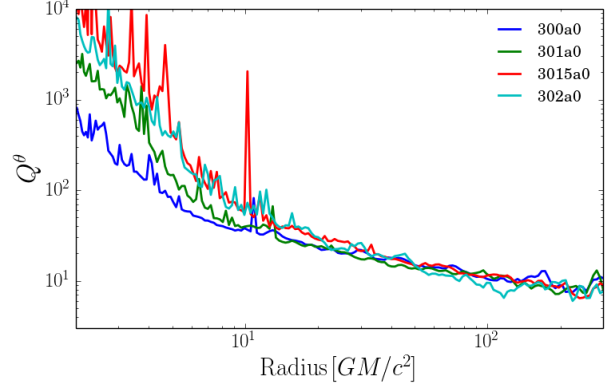


Figure 5. Vertically and time averaged MRI resolution parameter Q^θ .

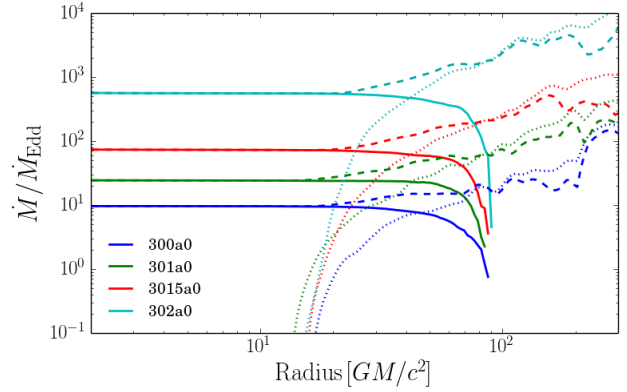


Figure 6. Radial profiles of the rest mass flux (accretion rate). Solid lines show the total flux, while dashed and dotted lines denote the fluxes of inflowing, and outflowing gas only, respectively.

black line shows the total flux of energy available at infinity obtained by summing up the MHD and radiative fluxes (T_t^r and R_t^r , respectively), and subtracting the rest mass energy flux (ρu^r), normalized by the rest mass energy flux through the BH horizon. The profile of the total energy flux is flat between the ISCO and the convergence radius $R \approx 60$, and corresponds roughly to efficiency of 4% — this fraction of $\dot{M}c^2$ is extracted by accretion and ejected as a sum of radiative flux, magnetic Poynting flux, and kinetic and thermal energies. This number is only slightly lower than the efficiency implied by the standard model of a radiatively efficient thin disk ($\eta_0 = 5.7\%$) and is roughly constant for all the $a_* = 0.0$ runs (see Table 2).

The total flux of energy can be decomposed into the MHD (magnetic, kinetic, and thermal components), and radiative (energy carried by photons) fluxes. At large radii the radiative flux dominates over the MHD flux because it consists of accumulated contributions of all the energy liberated by viscosity in the inner region. The radiative flux approaches $\dot{E}_{\text{rad}} = 0.03\dot{M}c^2$, what for accretion rate $\dot{M} \approx 10$, and radiative efficiency of a thin disk $\eta_0 \approx 0.06$ (Eq. 1), gives total radiative luminosity $L \approx 0.03 \times 10 / 0.06 L_{\text{Edd}} = 5 L_{\text{Edd}}$. The net radiative flux of energy changes sign inside $R \approx 20$, reflecting the fact that in this regions photons are effectively trapped and most of them are advected onto the BH. The departure of the total net energy flux from otherwise constant value $\sim 4\%$ inside ISCO is caused by rapidly increasing radial velocity of the flow in the plunging region, which increases the numerical diffusivity of

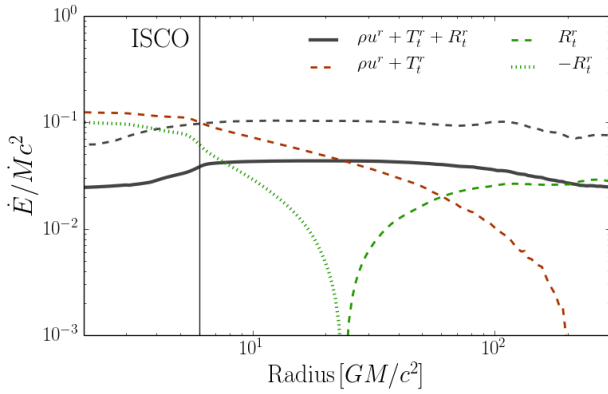


Figure 7. Radial profiles of the energy fluxes for simulation r300a0. The black solid line shows the flux of the total energy outflowing to infinity. Red and green lines show the MHD and radiative components, respectively. Dashed and dotted sections correspond to outflowing and inflowing energy flux, respectively. Dashed black line shows the total energy flux for run r300a9.

the scheme and introduces extra viscous contribution to the energy flux not reflected in the quantities that we plot.

More detailed discussion of disk luminosities is given in Section 3.4.2.

3.3.5 Magnetic field properties

The poloidal magnetic field is prevented from decaying by the sub-grid dynamo described in Appendix A. In all the models, we set the target magnetic field angle ξ_{dyn} (Eq. 29) to 0.25, and the magnetic to total pressure ratio β'_{damp} to 0.1. Figure 8 shows the radial profiles of the averages (vertical with density weight, and over time) of these two quantities. The dashed lines show the magnetic field angle ξ_{dyn} which was expected to settle down near 0.25. Indeed, for all runs and $R \gtrsim 10$ the mean magnetic field angle is close to that value. It departs from $\xi \approx 0.25$ only in the innermost region, where the magnetic field is determined by the rapidly accelerating and sheared gas. Solid lines in Figure 8 show the average ratio of magnetic to total pressure. Whenever it exceeds the prescribed critical value $\beta'_{\text{damp}} = 0.1$, the toroidal magnetic field is damped. Because of this asymmetry (no action is taken when $\beta'_{\text{damp}} < 0.1$) the resulting average β' is expected to be lower than 0.1. It is the case for the region outside $R \gtrsim 60$, where the pressure ratio for all the simulations is around $\beta' = 0.05$. Inside the inflow equilibrium region, the magnetic field component contributes more to the total pressure with decreasing radius. The typical value of that pressure ratio at $R = 10$ is 0.2–0.3. It exceeds the critical value of 0.1 because the damping of the toroidal component of magnetic field becomes less and less effective when the radial velocity (see Fig. 12) is large. The shear, which stretches the poloidal component of the magnetic field and amplifies the toroidal one, is unaffected by radial velocity. The sub-grid damping, however, acts on the orbital timescale (Eq. 33), and gas moving with larger velocity is affected by damping over a shorter time, making it less effective. The resulting profile of the magnetic pressure is, however, in qualitative agreement with 3D simulations of ADAFs (e.g., Narayan et al. 2012), which also show increased contribution of magnetic pressure towards the BH.

Figure 9 shows the radial profiles of the turbulent viscosity parameter α (Shakura & Sunyaev 1973). The dashed lines show the crude estimate, based on the product of the magnetic field angle

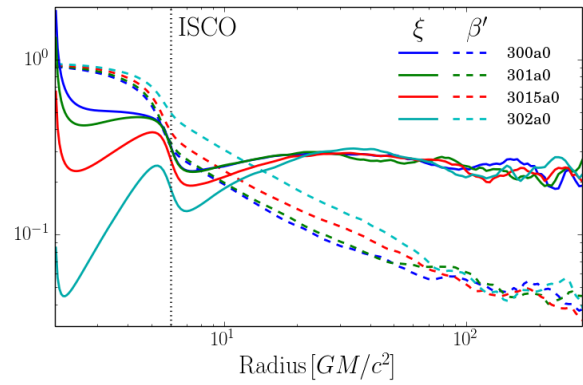


Figure 8. Average parameters of the magnetic field. The dashed lines show the magnetic to total pressure ratio, and the solid lines show the magnetic field angle (Eq. 29).

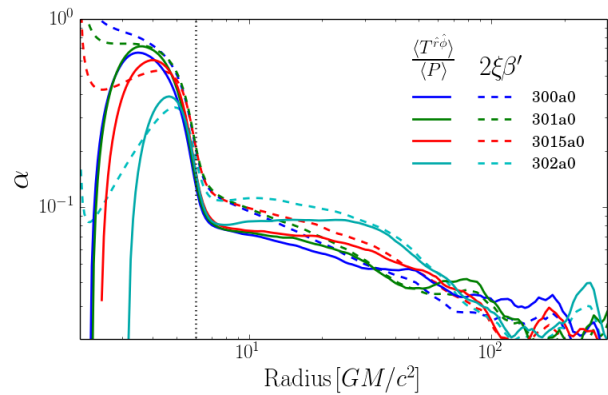


Figure 9. Profiles of the viscosity parameter α . Dashed lines show the estimate based on the product of the magnetic field angle and pressure ratio. Solid lines show the estimate of α calculated consistently.

and pressure ratio,

$$\alpha = \frac{\langle T^{\hat{r}\hat{\phi}} \rangle}{\langle p \rangle} \approx \frac{\langle b^r b^\phi \rangle}{\langle p \rangle} = \frac{\langle b^r b^\phi \rangle \langle b^2 \rangle}{\langle b^2 \rangle \langle p \rangle} = 2\langle \xi \rangle \langle \beta' \rangle, \quad (43)$$

while the solid lines show the viscosity parameter α estimated in a more consistent way directly through,

$$\alpha = \frac{\langle T^{\hat{r}\hat{\phi}} \rangle}{\langle p \rangle}, \quad (44)$$

where $T^{\hat{r}\hat{\phi}}$ is the orthonormal (r, ϕ) component of the gas stress-energy tensor in the mean comoving frame, and p is the total pressure. Following Penna et al. (2013b) we choose the azimuthal component of the gas velocity as the only non-zero component of the comoving frame at given location. The averages are taken as before, but this time only within one scale height of the disk to avoid strongly magnetized corona.

The two ways of estimating the viscosity parameter show good agreement. The α estimated with Eq. 44 has relatively flat profile between ISCO and $R \approx 60$, and falls in the range $\alpha = 0.06 \div 0.1$. It rapidly grows inside ISCO, reflecting the increase of the magnetic pressure, and falls down again when approaching the horizon. The whole profile is also in good qualitative agreement with the characteristics of α observed in 3D simulations, although the very rapid grow of α at ISCO is rather unphysical (Penna et al. 2013b).

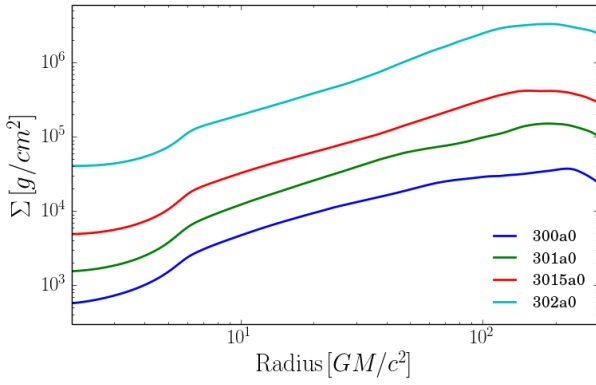


Figure 10. Radial profiles of the surface density.

3.3.6 Surface density, optical depth and velocities

Figures 10 and 12 show profiles of the surface density and radial velocity, respectively. Surface densities at given radius increase with accretion rates suggesting that the disk solutions correspond to the top, advection-dominated branch of slim disks on so-called S-curve diagrams (Abramowicz et al. 1988). Outside ISCO, surface density increases roughly proportionally to radius, what is also in good agreement with slim disk models (see e.g., Sądowski 2011).

Figure 11 presents radial profiles of the optical depth. The total optical depth, defined as,

$$\tau_{\text{tot}} = \int_0^\pi \rho(\kappa_{\text{es}} + \kappa_{\text{a}}) u^t \sqrt{g_{\theta\theta}} d\theta, \quad (45)$$

is shown with solid lines. Because scatterings strongly dominate over absorptions, the profiles of the total optical depth roughly correspond to the surface density profiles rescaled by $\kappa_{\text{es}} = 0.34 \text{ cm}^2/\text{g}$. Only close to the horizon the extra Lorentz factor u^t affects the scalings. For all the four simulations discussed here (r300a0 – r302a0) the total optical depth exceeds $\tau_{\text{tot}} = 1000$, making them very optically thick. They are, however, at the same time optically thin with respect to absorptions, because of high temperatures in the disk body. In this context, an important measure is the effective optical depth, which determines if a photon is absorbed along its scattering-affected path. We approximate the effective optical depth by calculating,

$$\tau_{\text{eff}} = \sqrt{(\tau_{\text{tot}} + \tau_{\text{abs}})\tau_{\text{tot}}}, \quad (46)$$

where τ_{abs} is the optical depth for absorption. The resulting profiles are plotted in Figure 11 with dashed lines. For the three runs with highest accretion rates, τ_{eff} exceeds 1 everywhere outside ISCO. Simulation r300a0, however, is effectively optically thin ($\tau_{\text{eff}} \lesssim 1$) inside $R \lesssim 10$. This fact may have significant impact on the emitted spectrum, but quantifying it will require detailed radiative transfer calculations.

Figure 12 shows profiles of the average radial velocity. All the simulations show very similar radial velocities which decrease with radius as R^{-2} , consistent with the slope obtained from simulations of non-radiative, optically thin disks (Narayan et al. 2012). However, there is a slight trend of decreasing radial velocity with accretion rate, which implies that the solutions are not completely in the ADAF regime where no dependence on accretion rate is expected.

Figure 13 shows radial profiles of the specific angular momentum. Outside $R \approx 10$, all the simulated disks show angular momentum corresponding to roughly 87% of the Keplerian angular

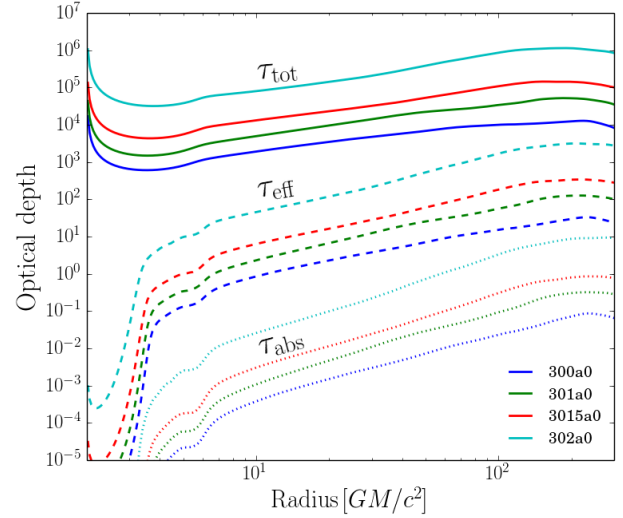


Figure 11. Radial profiles of the optical depth in simulations r300a0 – r302a0. Solid, dashed and dotted lines correspond to the total, effective, and absorption optical depths, respectively.

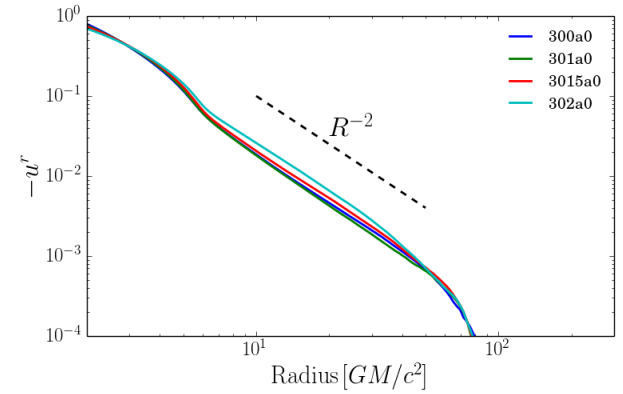


Figure 12. Radial profiles of the average radial velocity $\langle \rho u^r \rangle / \langle \rho \rangle$.

momentum. Inside $R \approx 10$ the profiles differ a bit, with the one corresponding to the lowest accretion rate (r300a0) being the closest to the Keplerian profile. Inside the ISCO, the angular momentum drops down for all the runs. This reflects the fact that viscosity in the plunging region is no longer regulated by the dynamo sub-grid model, and the α -viscosity parameter rapidly increases towards BH (Fig. 9).

3.3.7 Photosphere

Radiation generated by viscous dissipation is absorbed, re-emitted and scattered inside the bulk of the disk. However once a photon crosses the photosphere, it can escape to an observer located at infinity (the escape path follows a null geodesic).

In this subsection we are primarily interested in the location of the photosphere in the funnel region close to the axis. Here, gas flows out at considerable speed. Hence, the numerical solution achieves steady state out to quite a large radius. In many cases, inflow equilibrium is established out to the edge of the box (see the values of R_f in Table 2). Hence, we can follow the location of the

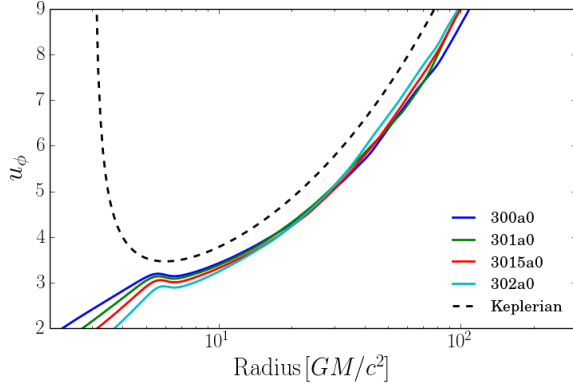


Figure 13. Radial profiles of the specific angular momentum u_ϕ .

photosphere to fairly large radii. In contrast, the discussion of disk properties close to the equatorial plane in previous subsections was limited to a much smaller range of radius $R \lesssim R_{\text{eq}} \approx 60$.

We estimate the radius R_{photo} of the photosphere in the funnel as a function of polar angle θ by integrating the optical depth from the outer boundary of the simulation box down towards the BH along fixed θ . In computing the optical depth, we need to allow for relativistic effects such as GR and motion of the gas. We make use of the fact that the opacity in any given frame scales as $1/\omega$, where ω is the frequency of the radiation as measured in that frame. We are interested in the opacity in the lab frame for an observer at infinity, whereas the opacities κ_{es} and κ_a correspond to the fluid frame. To carry out the transformation from one frame to the other, we model a radially outgoing light ray by an effective wavevector $k^\mu = (1, 1, 0, 0)$ and note that the frequency of the radiation as measured in a frame moving with four-velocity u^μ is equal to $-k^\mu u_\mu$. The optical depth at a given θ from any radius R inside the simulation box to the outer radius of the box $R_{\text{max}} = 5000$ is then given by

$$\tau_1(R) = - \int_R^{R_{\text{max}}} \rho(\kappa_a + \kappa_{\text{es}})(u_t + u_r) \sqrt{g_{rr}} dR', \quad (47)$$

where we use time-averaged quantities symmetrized with respect to the equatorial plane. Because $\tau_1(R)$ may significantly underestimate the opacity to infinity when R is close to R_{max} , we define a second measure of the opacity

$$\tau_2(R) = -[\rho(\kappa_a + \kappa_{\text{es}})(u_t + u_r) \sqrt{g_{rr}} R]_R. \quad (48)$$

We then estimate the photospheric radius $R_{\text{photo}}(\theta)$ at the given θ by the condition

$$\max(\tau_1(R_{\text{photo}}), \tau_2(R_{\text{photo}})) = 2/3. \quad (49)$$

Any value of R_{photo} which is larger than the maximum radius R_f of steady state in the funnel is discarded. Here, R_f is defined by the condition $R_f/v_r(R_f) = t/2$ where t is the duration of simulation data from which time-averaged quantities are obtained for calculating τ_1 , τ_2 (typically $t \sim t_{\text{max}}/2$, where t_{max} is given in Table 1).

Figure 14 shows the location of the photosphere for several of our simulated disk models. The red line corresponds to run r299a0 which accreted at $\sim 2\dot{M}_{\text{Edd}}$. Its photosphere is relatively close to the equatorial plane, but significantly above the disk density scale height (~ 0.2). The higher the accretion rate, the closer to the polar axis the photosphere is, and the more well-defined the optically thin funnel is. For run r301a0, the base of the funnel is at $z = 1000$, quite far from the BH, while for runs r3015a0 and r302a0, the

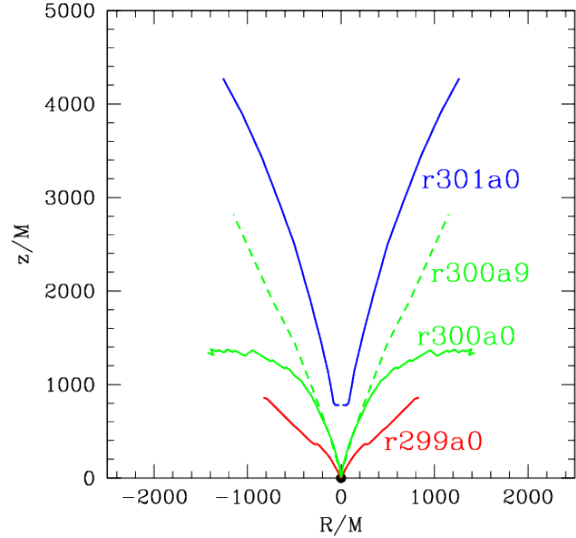


Figure 14. Profiles of the photosphere for disks with non-rotating BHs (solid lines), and simulation r300a9 ($a_* = 0.9$, dashed green line).

whole domain out to $R_{\text{max}} = 5000$ is optically thick at all θ . Hence these two models have no optically thin funnel within the simulation box. Note that the optical depth in the funnel is dominated by electron scattering. Only deep in the optically thick interior of the disk is absorption opacity important.

The dashed green line in Figure 14 shows the photosphere for run r300a9 which has a comparable accretion rate as run r300a0 but corresponds to a spinning BH with $a_* = 0.9$. Here the photosphere is located significantly closer to the polar axis. This reflects the fact that disks with spinning BHs eject stronger winds (see next Section) and thus tend more easily to fill the funnel region with optically thick outflowing gas.

3.4 Super-critical disks around rotating BHs

In addition to the four runs with non-rotating BHs discussed in the previous section, we performed a set of three simulations with BH spin parameter $a_* = 0.9$. One of the most exciting aspects of accretion disks around rotating BHs is the possibility of ejecting jets through the Blandford-Znajek mechanism (Blandford & Znajek 1977; Penna et al. 2013c; Lasota et al. 2014). It has been shown both in 2D and 3D that super-critical, optically thick disks can produce jets with very similar efficiencies to radiatively inefficient, optically thin disks (Sądowski et al. 2013a; McKinney et al. 2013). An open question is how effective is jet production for accretion disks accreting at accretion rates comparable to and below the Eddington limit. In this paper we do not specifically address this question, but study general properties of outflows from axisymmetric accretion disks supported by sub-grid dynamo.

We start with comparing two simulations initiated with the same torus, and the same initial magnetic field, but evolved with different values of BH spin (runs r300a0 and r300a9). Figure 15 compares the net, inflow and outflow accretion rates. The solid lines denote the net rest mass flux and show that both simulations accrete at roughly the same level³. However, there is significant difference in the inflowing and outflowing fluxes. While for the $a_* = 0$ run, the

³ In terms of the Eddington accretion rate units defined in Eq. 1. The abso-

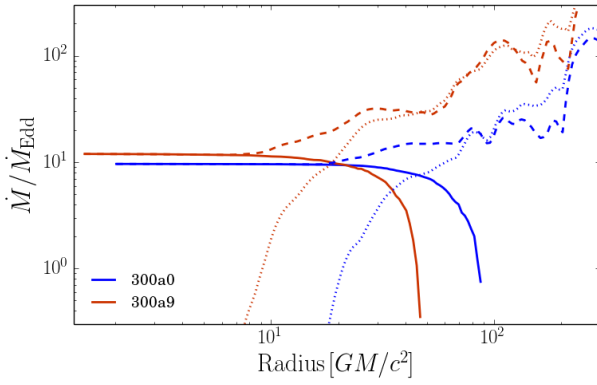


Figure 15. Similar to Fig. 6 but for two, otherwise identical, runs with different BH spin. Blue and red lines correspond to runs `r300a0` and `r300a9`, respectively.

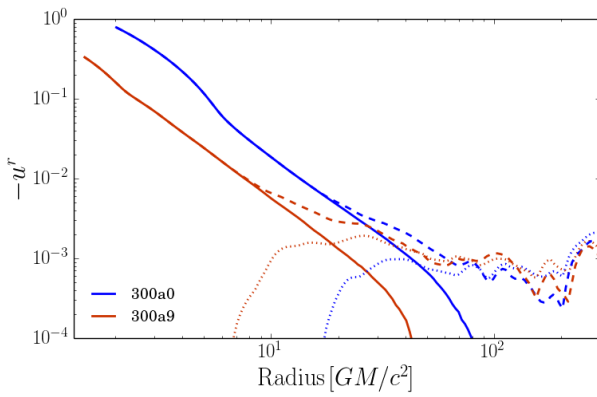


Figure 16. Net (solid), inflowing (dashed) and outflowing (dotted) radial velocities. Blue and red lines correspond to runs `r300a0` and `r300a9`, respectively.

gas is lost on the way towards the BH only down to $R \approx 20$, in case of the spinning BH outflows occur down to $R \approx 10$. This is consistent with results obtained earlier both for optically thin ADAFs, and super-critical optically thick disks (Sądowski et al. 2013b, 2014), and results from BH spin impact on the spacetime, which also implies the location of ISCO much closer to the horizon for $a_* = 0.9$.

Figure 16 compares radial velocities in the two runs. The net inward radial velocity is significantly smaller for the run with spinning BH. This results mostly from the fact that although the dynamo parameters were set in exactly the same way, the resulting α viscosity parameter for the $a_* = 0.9$ run is roughly 30% lower than for the non-rotating BH case (the inflow velocity is expected to be proportional to α). Additionally, the magnetic flux accumulated at the horizon (although relatively small, as will be discussed in a moment), contributes significantly to the outflowing energy flux (compare solid and dashed black lines in Figure 7) because of the Blandford-Znajek process, slowing the inflowing gas down.

lute accretion rate is larger for `r300a0` by the ratio of thin disk efficiencies $\eta_0(a_* = 0.9)/\eta_0(a_* = 0) = 2.74$.

3.4.1 Magnetic field and accretion efficiency

The efficiency of the energy extraction from a rotating BH through the Blandford-Znajek process depends mostly on the BH spin and the magnetic flux accumulated on the horizon. It is often characterized by the magnetic flux parameter φ (Eq. 39) shown in Figure 16 for runs with $a_* = 0.9$. The first two panels correspond to simulations initiated with a single poloidal loop of magnetic field. As a result, the magnetic flux accumulates at the horizon more efficiently than for simulations initiated with a quadrupolar magnetic field (bottommost panel and Figure 3). From the two simulations initiated with a single loop, magnetic flux accumulates much faster for run `r302a9madhb` which had stronger initial seed magnetic field. We stopped that simulation once the φ parameter exceeded $\varphi = 50$, which corresponds to the Magnetically Arrested Disk (MAD) limit which cannot be simulated properly in axisymmetry⁴.

The definition of the parameter φ does not discriminate between the topology of the magnetic field, as it integrates the absolute value of the radial component of the magnetic field over the horizon. To get insight into the topology of the magnetic field crossing the horizon we define parameter φ_{dip} ,

$$\varphi_{\text{dip}} = \frac{1}{\sqrt{\langle \dot{M} \rangle}} \frac{4\pi}{2} \int_0^\pi \int_0^{2\pi} \sqrt{-g} B^r \text{sign}(\theta - \pi/2) d\varphi d\theta, \quad (50)$$

For a perfectly dipolar magnetic field at the horizon one has $|\varphi_{\text{dip}}| = \varphi$. For a quadrupolar (or any even-polar) magnetic field, $\varphi_{\text{dip}} = 0$. This parameter is plotted with dashed lines in Figure 17. For simulations `r302a9mad` (top panel, initiated with a single loop of weak magnetic field) and `r300a9` (bottom panel, initiated with multiple loops), φ_{dip} oscillates around zero showing that the magnetic field at the horizon is close to quadrupolar, and that it often flips orientation. This is because the dynamo generates turbulent magnetic field and, in case of simulation `r302a9mad`, quickly overwhelms the initial dipolar field. For run `r302a9madhb` (middle panel), on the contrary, φ_{dip} stays all the time close to φ , and does not change sign, because the magnetic field at the horizon is purely dipolar. This results from stronger initial magnetic field which is not so easily overwritten by dynamo-generated turbulent field.

To study how the amount of energy outflowing from the system depends on the magnetic flux threading the horizon, we took for each simulation snapshots spaced every $\Delta t = 50$, and extracted the accretion efficiency, defined as,

$$\eta = \frac{\int_0^\pi (\rho u^r + T_r^t + R_r^t) \sqrt{-g} d\theta}{\int_0^\pi \rho u^r \sqrt{-g} d\theta}, \quad (51)$$

where the integrals are taken at $R = 15$ (to avoid the departure from the constant energy flux close to the BH). Figure 18 shows this quantity against the magnetic flux at the horizon parameter φ (Eq. 39). Colors of points denote the time each data point corresponds to. For the two strongly magnetized runs (`r302a9mad` and `r302a9madhb`, first two panels) the points cluster along $\propto \varphi^2$ line (but for the very initial dark blue points), what is consistent with the prediction of the Blandford-Znajek power (see e.g., Penna et al. 2013c). The vertical spread of points below that line is significantly smaller for purely dipolar run `r302a9madhb`. The bottom panel corresponds to simulation `r300a9` which has never accumulated

⁴ In 3D gas can make its way through the accumulated magnetic field by breaking axisymmetry via an interchange instability, (e.g., Li & Narayan 2004), but this is not possible in 2D. Hence 2D simulations cannot be trusted once they reach the MAD limit.)

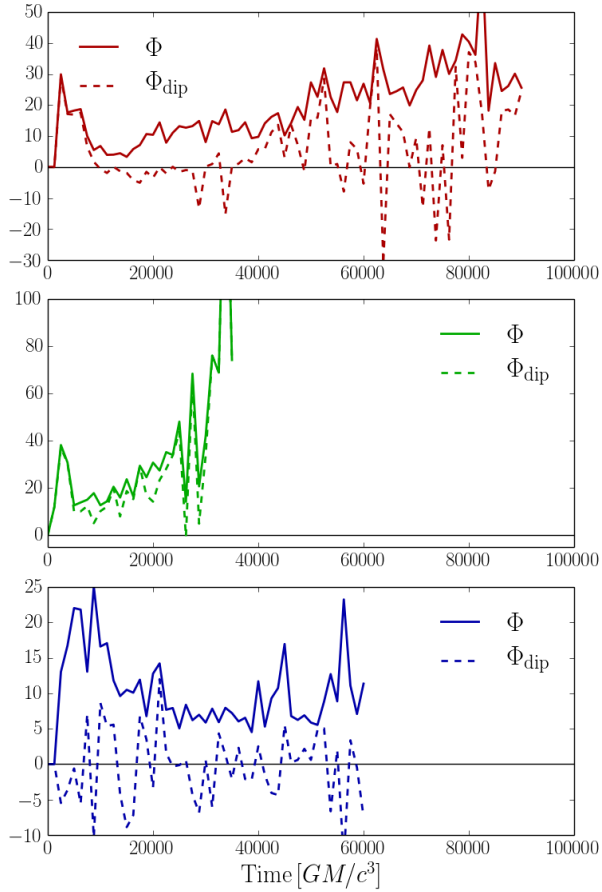


Figure 17. Total (φ , Eq. 39) and dipolar (φ_{dip} , Eq. 50) magnetic flux parameter calculated at the BH horizon for runs (top to bottom) r302a9mad, r302a9madhb, and r300a9.

significant magnetic field. As the result the φ parameter never significantly exceeds $\varphi = 20$, and the accretion efficiency remains relatively low, but still larger than for the corresponding run r300a0 (Fig. 7). Because the energy output due to the Blandford-Znajek process is often in this case comparable with the accretion-related (which for a thin disk with $a_* = 0.9$ equals $\eta_0 = 0.156$), the spread of points in the bottom panel of Figure 18 is significant.

To assess if the energy outflow depends on the topology of the magnetic field crossing the horizon, we plot in Figure 19 the energy output normalized by φ^2 (which quantity has a flat distribution) as a function of quantity parametrizing the field topology, which we define as,

$$\mathcal{T} = 1 - |\varphi_{\text{dip}}|/\varphi. \quad (52)$$

Purely dipolar and quadrupolar fields give $\mathcal{T} = 0$ and $\mathcal{T} = 1$, respectively. Figure 19 suggests that there is a weak dependence of the energy outflow on the topology of the magnetic field. Dipolar magnetic field on average produces stronger energy output, but purely quadrupolar field results in significant energy outflow as well.

3.4.2 Luminosity

In the standard model of a thin accretion disk, the whole gravitational energy liberated by viscosity is immediately transported by diffusion to the disk surface and emitted as radiation. As a result,

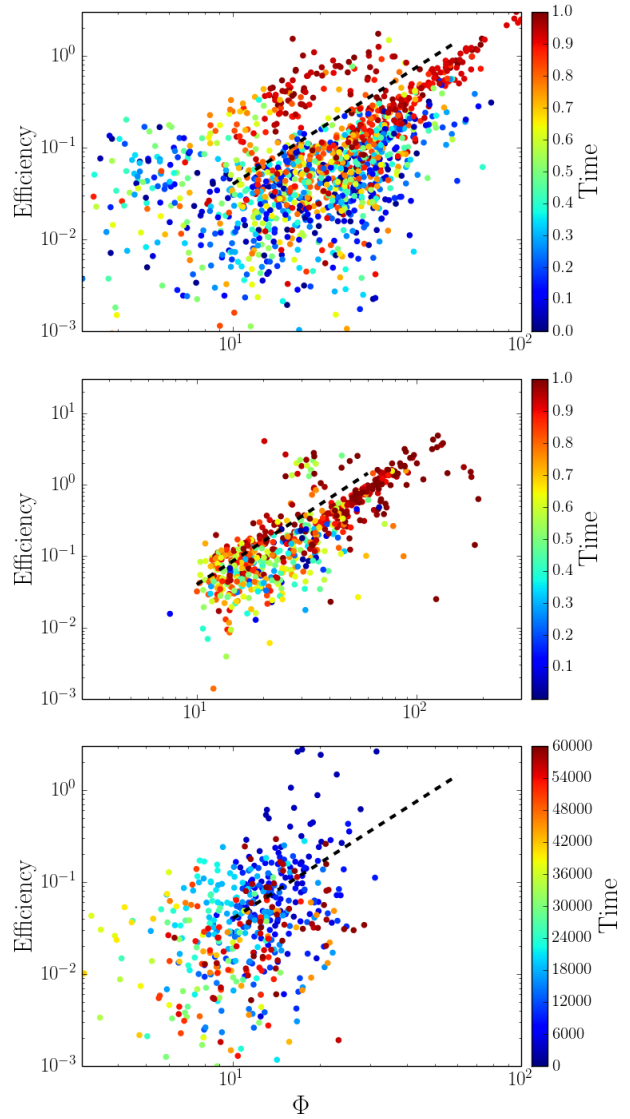


Figure 18. Efficiency of jet as a function of magnetic flux parameter for runs (top to bottom) r302a9mad, r302a9madhb, and r300a9. Points correspond to snapshot data taken every $\Delta t = 500$. Colors denote the time. Jet power was calculated at $R = 15$. The dashed lines show the expected φ^2 dependence.

the total (integrated over radius and frequency) radiative flux corresponds to the thin disk efficiency which depends only on the binding energy of gas at the disk inner edge (Eq. 2). The luminosity of a thin disk is therefore given by,

$$L_{\text{thin}} = \eta_0 \dot{M} c^2. \quad (53)$$

Introducing the Eddington accretion rate (Eq. 1), we also have,

$$\frac{L_{\text{thin}}}{L_{\text{Edd}}} = \frac{\dot{M}}{\dot{M}_{\text{Edd}}}. \quad (54)$$

Thin disks are radiatively efficient. According to the standard analytical modeling, it is no longer true when accretion rate is large, and the advective contribution to cooling is important. Such disks are called “slim” (Abramowicz et al. 1988), and their efficiency significantly drops down because photons can effectively be advected on the BH, instead of being radiated away.

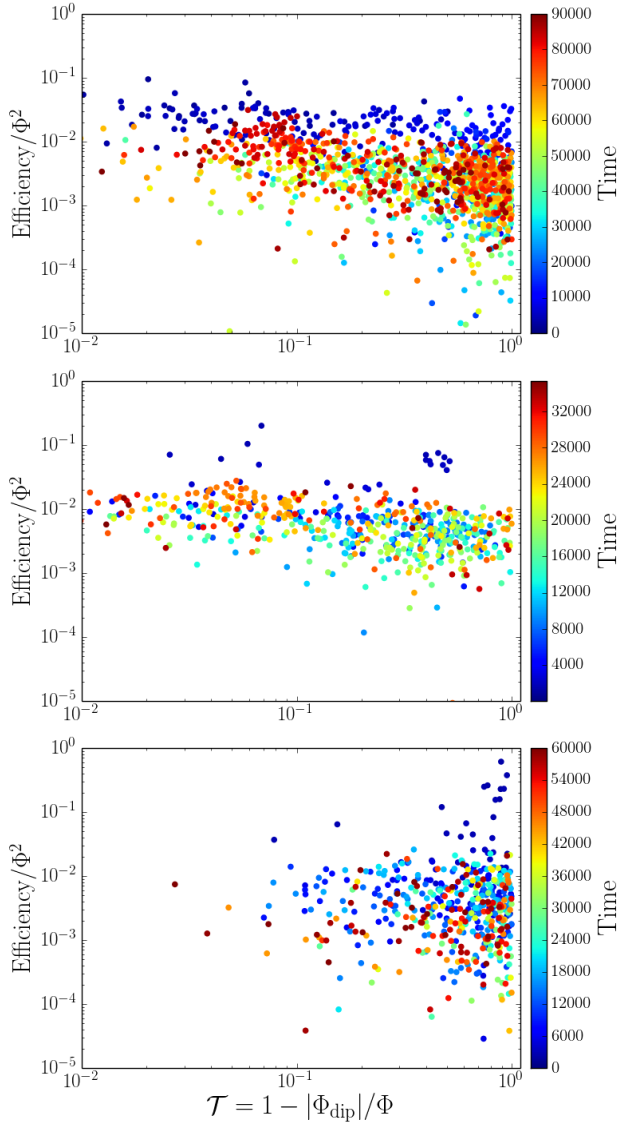


Figure 19. Jet power reduced by square of the magnetic flux as a function of the dipolar parameter $\mathcal{T} = 1 - \varphi_{\text{dip}}/\varphi$ for runs (top to bottom) r302a9mad, r302a9madhb, and r300a9.

Simulations of radiative, turbulent accretion disks show that the above picture is over-simplified. Because of the turbulent structure of the disk, other means of energy transport, e.g., magnetic buoyancy, convection, may be important. Energy is also carried out by jets or winds, which is not taken into consideration in analytical disk models. Finally, analytical models rely on separating the radial and vertical structure equations, but this separation becomes questionable when the disk is geometrically thick. Detailed study of the energy transport inside global accreting disks is extremely interesting, but is not within the scope of this paper. In this section we limit ourselves to discuss various measures of the disk luminosities.

The most fundamental measure of the amount of energy extracted by accretion is the flux of “energy at infinity”, i.e., the flux of kinetic, internal, and radiative energies that can be deposited into the interstellar or intergalactic medium. The total flux of “energy at infinity” is,

$$L_{\text{tot}} = 2\pi \int_0^\pi (\rho u^r + T_r^r + R_r^r) \sqrt{-g} d\theta, \quad (55)$$

and the corresponding accretion efficiency,

$$\eta_{\text{tot}} = \eta_0 \frac{L_{\text{tot}}}{L_{\text{Edd}}} \frac{\dot{M}_{\text{Edd}}}{\dot{M}}. \quad (56)$$

Generally speaking, the total energy flux equals to the average specific energy (Bernoulli number) of the gas falling through the horizon. This is the quantity we considered in Section 3.4.1 (we evaluated it at a specific radius: $R = 15$).

Another measure of luminosity that is important from the observational point of view is the radiative luminosity, i.e., the flux of energy carried by photons to an observer. However, extracting this quantity from numerical simulations like ours is not straightforward. Ideally, one would like to know the disk equilibrium solution in the whole region extending from the BH horizon to the photosphere surface. As Figure 14 shows, the photosphere in the super-critical disks forms optically thin funnel near the axis, but extends far near the equatorial plane. Infact, the location of the photosphere near the equatorial plane is determined by the extent of the initial torus (Fig. 1), and the dynamics of gas ejected from its surface. Because of the limited duration of simulations, the inflow/outflow equilibrium is reached only within $R \lesssim 60$ near the equatorial plane — anything outside this radius is not consistent with the accretion solution, and rather reflects the initial state of each simulation. Therefore, calculating the radiative luminosity by integrating the radiative flux over the solid angle near the outer boundary would be meaningless. What is more, the outer radius adopted in this work, $R_{\text{out}} = 5000$, is still not enough to encompass the whole photosphere for the highest accretion rates.

For these reasons, when calculating the radiative luminosity, we limit the range of integration over θ to the optically thin funnel region. Photons that entered this region are expected to reach the observer because of low optical depth along the line of sight. In this way, this measure of luminosity, calculated as,

$$L_{f,\text{rad}} = 2\pi \int_{\text{funnel}} R_f^r \sqrt{-g} d\theta, \quad (57)$$

may be interpreted as the lower limit of radiative luminosity (photons may diffuse into the optically thin funnel from the optically thick wind beyond the boundaries of the domain). For completeness, we calculate also the total energy flux in the funnel region,

$$L_{f,\text{tot}} = 2\pi \int_{\text{funnel}} (\rho u^r + T_r^r + R_r^r) \sqrt{-g} d\theta. \quad (58)$$

We evaluate both of these quantities at the limiting radius of steady state $R = R_f$ (see Table 2 for values). The corresponding efficiencies are calculated in a similar way to Eq. 56. Knowing the luminosity inside the optically thin region we may also calculate the average radiative flux there in units of the isotropic Eddington flux, $F_{\text{Edd}} = L_{\text{Edd}}/4\pi R^2$,

$$\frac{F_{f,\text{rad}}}{F_{\text{Edd}}} = \frac{1}{1 - \cos \theta_f} \frac{L_{f,\text{rad}}}{L_{\text{Edd}}}, \quad (59)$$

where θ_f is the opening angle of the funnel.

These three measures of luminosity, together with the measure of the radiative flux in the funnel for the same BH spin and accretion rate are given in Table 2. The numbers in brackets give the corresponding efficiencies. For comparison, the radiative luminosities and efficiencies of the analytical thin and slim disk models are also listed.

The third column in Table 2 gives the total luminosity, L_{tot} . All the simulations with a non-rotating BH show consistent accretion efficiency, $\eta_{\text{tot}} = 0.043 \div 0.049$ (that fraction of the accreted rest

Table 2. Accretion disk luminosities

Model	\dot{M}	$L_{\text{tot}} (\eta_{\text{tot}})$	$L_{f,\text{tot}} (\eta_{f,\text{tot}})$	$L_{f,\text{rad}} (\eta_{f,\text{rad}})$	$F_{f,\text{rad}}$	$L_{\text{thin,rad}} (\eta_{\text{thin,rad}})$	$L_{\text{slim,rad}} (\eta_{\text{slim,rad}})$	R_f
r302a0	559	456 (0.046)	-	-	-	559 (0.057)	12.1 (0.001)	-
r3015a0	73.1	55.4 (0.043)	-	-	-	73.1 (0.057)	9.0 (0.007)	-
r301a0	24.3	19.0 (0.045)	5.39 (0.013)	1.50 (0.004)	39.1	24.3 (0.057)	6.7 (0.016)	4800
r300a0	9.6	7.31 (0.043)	3.45 (0.020)	2.11 (0.013)	7.19	9.6 (0.057)	4.6 (0.027)	2000
r299a0	2.1	1.81 (0.049)	1.80 (0.049)	1.65 (0.045)	6.53	2.1 (0.057)	1.8 (0.049)	1200
r302a9madhb	3050	5080 (0.260)	527 (0.027)	240 (0.012)	5100	3050 (0.156)	12.9 (0.0007)	4700
r302a9mad	2060	3290 (0.249)	176 (0.013)	110 (0.008)	19000	2060 (0.156)	12.7 (0.001)	4700
r300a9	11.9	7.93 (0.104)	4.33 (0.057)	2.60 (0.034)	37.6	11.9 (0.156)	5.2 (0.068)	3200

Accretion rates, luminosities, and fluxes are given in the Eddington units; numbers in brackets give the accretion efficiency, $\eta = L/Mc^2$,

L_{tot} - total energy flux measured at $R = 15$,

$L_{f,\text{tot}}$, $L_{f,\text{rad}}$ - respectively total and radiative energy flux measured at R_f within the optically thin funnel,

$F_{f,\text{rad}}$ - average radiative flux inside the optically thin region measure at R_f ,

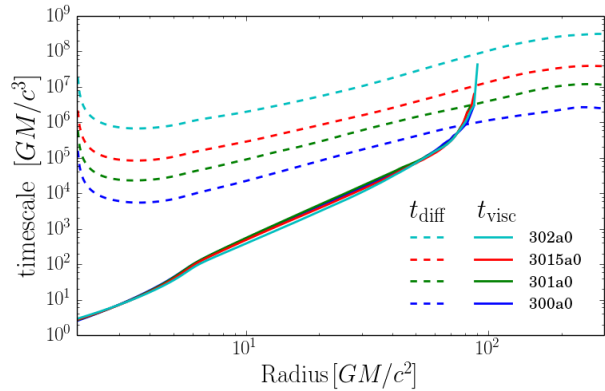
$L_{\text{thin,rad}}$, $L_{\text{slim,rad}}$ - radiative luminosities of a thin and slim disk (Sądowski 2009), respectively, with given BH spin and accretion rate.

mass energy is liberated in all other forms of energy). This number is slightly lower than the thin disk efficiency ($\eta_0 = 0.057$) and indicates that gas falls onto the BH with slightly higher specific energy than the one corresponding to test particles at ISCO. The efficiency of simulated disks is significantly higher than the efficiency of slim disks which predict significant drop in efficiency with increasing accretion rate (down to $\eta_{\text{slim}} = 0.001$ for $\sim 500\dot{M}_{\text{Edd}}$) due to the photon trapping and advection. This fact results from the presence of outflows in the numerical simulations, which are ignored in the slim disk approach.

The total accretion efficiencies for the runs with spinning BHs are significantly higher because of the extra source of energy — the Blandford-Znajek mechanism extracting the rotational energy of the BH. The two runs initiated with single loop of magnetic field (r302a9madhb and r302a9mad) have higher efficiencies than the one initiated with multiple quadrupolar loops (r300a9) because they managed to accumulate more magnetic flux at the horizon (Fig. 17). The exact values of these efficiencies depend on the average magnetic flux parameter in the period of time used for averaging ($\varphi \approx 25$ for r302a9madhb and r302a9mad).

The fourth and fifth columns of Table 2 show the total and radiative efficiencies measured by integrating the corresponding energy fluxes inside the optically thin funnel at some large radius R_f (given in the last column). The two simulations with the highest accretion rates were so optically thick that there was virtually no photosphere inside the simulation domain. The other three runs with a non-rotating BH show that the larger the accretion rate (and narrower the funnel), the smaller fraction of the total and radiative energy fluxes escapes through the funnel. The remaining part flows out in the optically thick region of outflow, and may ultimately cross the photosphere (outside of the simulation domain), or get absorbed by the gas increasing its thermal or kinetic energies. In the case of the run r299a0, accreting at the lowest rate ($2.1\dot{M}_{\text{Edd}}$), nearly all the energy escapes through the funnel, mostly in form of the radiative flux. The simulations with spinning BHs show that the efficiencies of the energy fluxes in the funnel are significantly lower than the net efficiencies (η_{tot}), reflecting the fact that most of the energy is bound in an outflowing optically thick wind.

Although the radiative luminosities in the funnel are moderate for the non-rotating BH disks, the effective flux of radiation in the funnel (sixth column in Table 2) significantly exceeds the Eddington value because of the small solid angle covered by the radiative flux there. Already for simulation r299a0 ($\dot{M} = 2.1\dot{M}_{\text{Edd}}$) the effective flux exceeds the isotropic Eddington flux more than six times. The fluxes are even higher for the simulations with a spinning BH,


Figure 20. Viscous and diffusive timescales for the four super-critical disks.

where the radiative flux in a narrow funnel is amplified by spin-related extra energy outflow.

Very large optical depths would imply effective photon trapping. In Figure 20 we compare the viscous timescale,

$$t_{\text{vis}} = -\frac{R}{u^r}, \quad (60)$$

where u^r is the average inflow velocity, with the photon (vertical) diffusion timescale,

$$t_{\text{diff}} \approx 3\tau_{\text{tot}}H, \quad (61)$$

where τ_{tot} and H are the total vertical optical depth, and disk density scaleheight, respectively. The fact that the viscous timescale is significantly shorter suggests that most of the photons inside the disk are trapped and effectively advected inward (the solutions are advection-dominated). Indeed, Figure 7 shows that the net trapping radius for photons is located at $R \approx 20$. Despite effective photon trapping, the disk is able to liberate significant fraction of the accreted rest mass energy. Therefore, the energy dissipated by viscosity must be efficiently transported outward by other processes. Outflows ejected by magnetic fields most likely play a crucial role. Detailed investigation of the means of energy transport will be done in one of the following works.

3.5 Unstable thin disks

In previous sections we discussed simulations of disks around both rotating and non-rotating BHs, accreting at rates exceeding the Eddington limit. The ultimate accretion rate of a given disk was de-

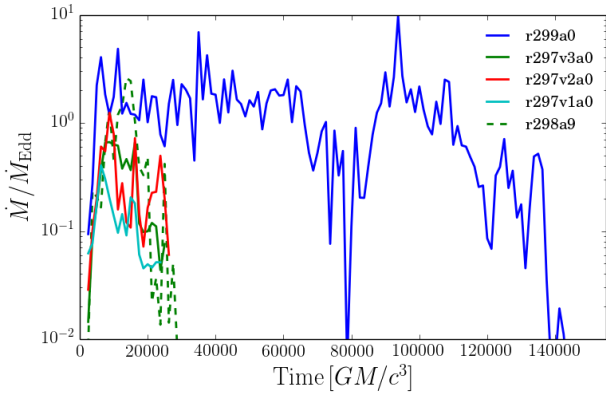


Figure 21. Accretion rate history for the unstable thin disks.

terminated by the density of the initial equilibrium torus. It is therefore straightforward to attempt to simulate disks accreting at lower rates, comparable and lower than the Eddington limit. One would expect, based on the standard thin disk theory, that such disks would be thinner, colder, and accreting with lower velocities. Simulating them would be also more challenging — thinner disks require smaller grid cells near the equatorial plane what suppresses the time step, and lower radial velocities imply longer viscous timescales, requiring longer, more expensive simulations. What is more, once the accretion rate drops below $\sim 5\dot{M}_{\text{Edd}}$ (Sądowski 2011), disk solutions are expected to leave the slim disk branch, and enter the thermally unstable regime of radiation pressure dominated, radiatively efficient disks.

To our knowledge, so far only Ohsuga & Mineshige (2011) attempted to simulate such thin accretion disks with an MHD code. However, the thin disk model described there was not supported by dissipative heating — the lack of resolution suppressed the MRI, and the disk collapsed because of insufficient heating rate.

Simulating thin accretion disks is for these reasons very challenging and expensive. It is clear that in the near future no 3D MHD simulation could even approach simulating disks with accretion rates $\dot{M} \sim 0.1\dot{M}_{\text{Edd}}$. This may be feasible, however, in axisymmetry with sub-grid dynamo, which allows for long lasting simulations. In this section we describe our first attempt to resolve sub-critical, geometrically thin disks.

We performed five simulations initiated with torus densities lower than for the simulations described so far (Table 1). Four of them were simulated with a non-rotating BH, and one with BH spin $a_* = 0.9$. Figure 21 shows the accretion rate history for these simulations. All runs but for r299a0 quickly ceased accreting gas after a short (lasting $\sim 10,000 GM/c^3$) episode of efficient accretion with $\dot{M} \sim 0.1 \div 1.0\dot{M}_{\text{Edd}}$. Only run r299a0 managed to accrete gas consistently for a longer period of time. Until $t = 60,000$, the accretion rate oscillated around $2.1\dot{M}_{\text{Edd}}$. Afterwards, it went down, only to come back to the original value around $t = 90,000$, and finally showed rapid decrease and ceased at $t = 140,000$.

Figure 22 shows snapshots of density in run r299a0 at various moments of time. The topmost panel corresponds to the episode of continuous accretion at $t < 60,000$, and shows a relatively thin (density scaleheight at $H/R \approx 0.2$), turbulent accretion disk. At $t = 75,000$ (second panel), corresponding to the first dip in the accretion rate, the innermost part of the disk was significantly thinner and denser. At $t = 100,000$, when the accretion rate was again consistent and around $2\dot{M}_{\text{Edd}}$, the disk looked exactly as in the topmost panel. This was followed by another decrease in accretion rate, and

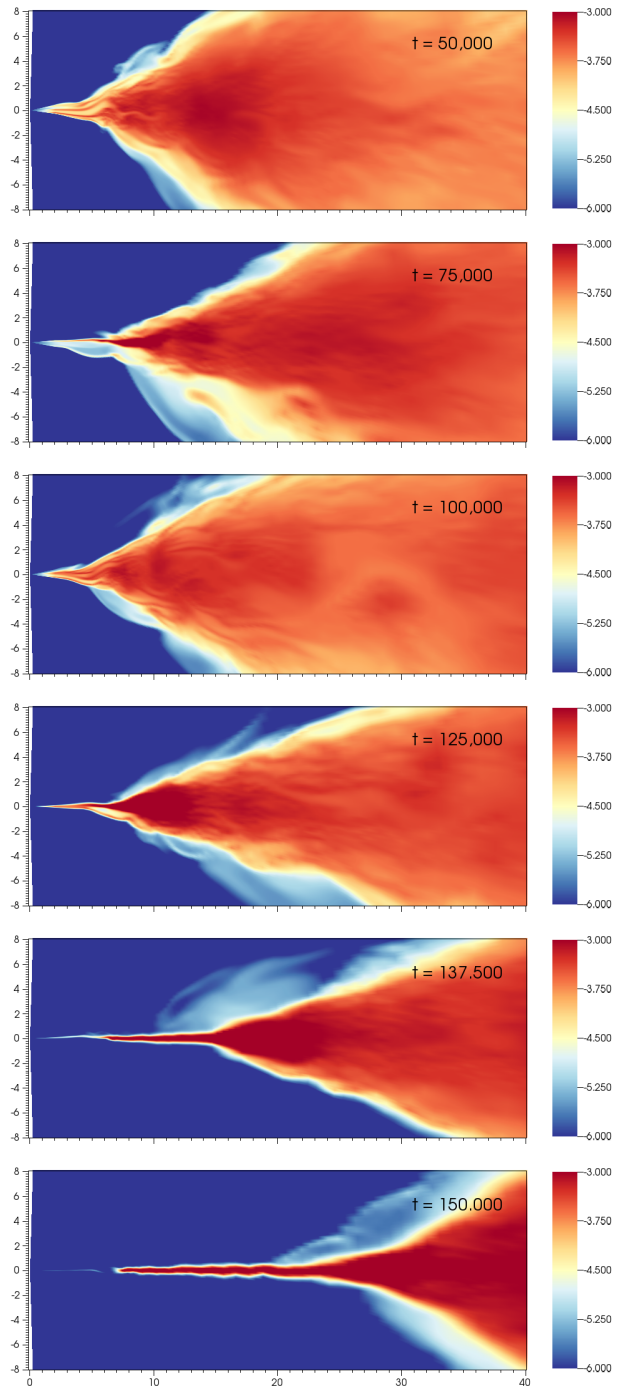


Figure 22. Sequence of snapshots of logarithms of density for run r299a0 showing the collapsing disk. The snapshots correspond to (top to bottom): $t = 50,000, 75,000, 100,000, 125,000, 137,500,$ and $150,000$.

corresponding compression of the innermost region ($t = 125,000$). This time, however, the disk did not manage to recover its original state, and, as the two bottom-most panels of Figure 22 show, collapsed to a very thin and high density state. At that point, the vertical resolution, although already extremely high, was not enough to sustain turbulence, MRI ceased, and accretion stopped.

Figure 24 shows the evolution of disk thickness and mean temperature at fixed radius $R = 15$ for the four collapsing runs around

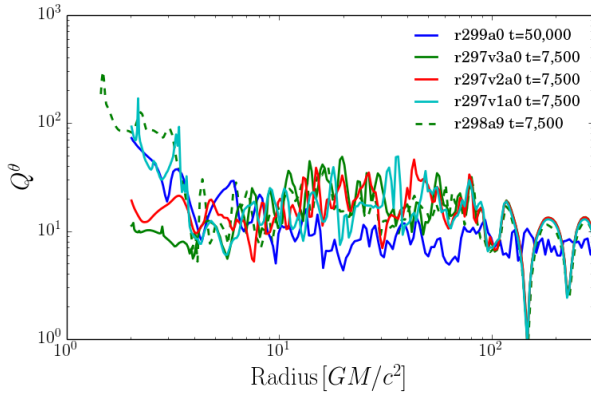


Figure 23. Vertically averaged MRI resolution parameter Q^θ for the unstable disks at $t = 50,000$ (for r299a0) or $t = 7,500$ for the other runs.

non-rotating BHs. All the runs show initial increase of thickness and temperature before $t = 10,000$ from values intrinsic to the initial torus, towards the values corresponding to a turbulent, accreting flow. Only run r299a0 manages to sustain that state for significant time. The temperature and disk thickness are correlated with each other for all the runs. The evolution of run r299a0 suggests that drop in temperature precedes decrease of disk thickness. This fact suggests, that disk thickness adjusts to the pressure in the disk to maintain vertical hydrostatic equilibrium. Ultimately, run r299a0 shows runaway cooling and collapses, as the other runs did much earlier.

Such runaway cooling could take place because of insufficient resolution leading to not resolving MRI, and effectively suppressing the heating rate. To reject this possibility we show the MRI resolution parameter Q^θ (Eq. 42) in Figure 23 at times directly preceding the collapse for each of the five runs. Values of Q^θ in the innermost ($R < 10$) region, where the collapse begins, fall in range $7 \lesssim Q^\theta \lesssim 30$, and suggest that MRI is properly resolved there. To further verify that our choice of resolution is enough we performed two additional simulations similar to run r298a0 but with nearly doubled the resolution in the polar angle for one run, and in radius for the other. They both showed exactly the same behavior.

The accretion rates of these five runs (Fig. 21) suggest that they belong to the thermally unstable branch of solutions, outside the region where advective cooling can act to stabilize against thermal collapse. For a radiation pressure dominated radiatively efficient disk with α -viscosity, the heating rate ($Q^+ \propto \alpha p_0 H \propto p_0^2$) has a steeper dependence on the midplane total pressure p_0 (at fixed surface density and α viscosity parameter) than the radiative cooling rate ($Q^- \propto T^4 \propto p_0$). This fact inevitably leads either to a local runaway collapse or expansion of the disk, and may trigger a large scale evolution of the disc structure (limit cycle) similar to the one seen in dwarf nova outbursts (see Lasota 2001, for a review). The fact that run r299a0 shows significantly less rapid collapse may be explained by the fact that its accretion rate is very close to the turnover point at $\sim 5\dot{M}_{\text{Edd}}$. We believe that this mechanism is behind the collapse observed in our simulations. More detailed study of the energy balance is beyond the scope of this paper.

One of the major puzzles in our understanding of BH accretion disks is the fact that the thermal instability suggested by the α -viscosity model (and seen in our simulations) does not take place for most, if not all of the BH binaries, which show steady lightcurves even for luminosities corresponding to the unstable range of accretion rates. Most tempting explanation would be to say

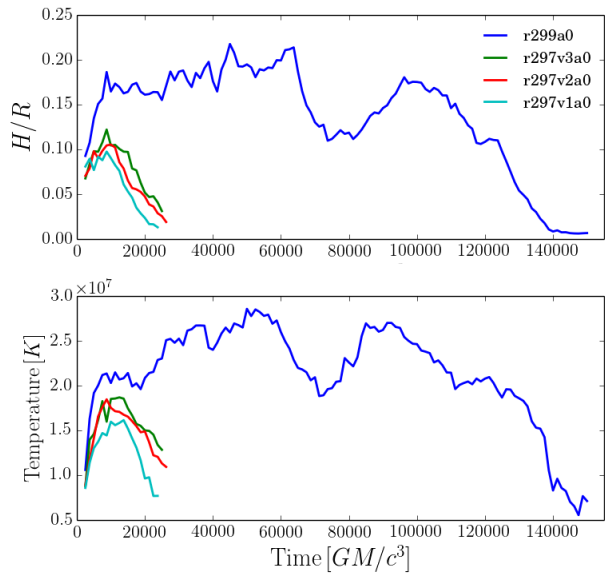


Figure 24. Changes with time of disk H/R ratio (top panel) and mean temperature (bottom) measured at radius $R = 15$ for the collapsing thin disk models with $a_* = 0.0$.

that the assumption that α -viscosity properly described the viscous stress-energy tensor arising from MRI-driven turbulence is wrong. This could be verified by performing local simulations of vertically stratified, radiation-pressure dominated gas. Initial work by Hirose et al. (2009a), performed with the flux-limited diffusion radiative transfer scheme, suggested that turbulent flows in this regime are indeed thermally stable. However, Jiang, Stone, & Davis (2013) repeated their study using improved radiative closure, and showed that the stability is affected not only by the way the radiation is treated, but also by the size of the box considered. For their most reliable setup, the disk annuli was shown to be thermally unstable. Therefore, the puzzle remains open.

One has to keep in mind, that although the dynamo-sustained turbulence that characterizes our axisymmetric accretion disks has mean properties similar to the 3D turbulence, some aspects of it, e.g., response to compression, may be different from properties of 3D turbulence. Therefore, to study thermal stability self-consistently, one has to ultimately perform 3D simulations. Our model may provide only limited insights into this issue.

4 SUMMARY AND DISCUSSION

In this paper we have introduced a new sub-grid prescription for the magnetic dynamo that allows axisymmetric simulations of accretion disks to be run for arbitrarily long times. The dynamo model generates a weak correction to the global poloidal field, and drives it towards the properties of a 3D saturated turbulent state, namely, the proper value of the magnetic field angle (Eq. 29) and magnetic to total pressure ratio (Eq. 30). We have implemented the dynamo model into a radiative, general relativistic, ideal MHD code KORAL. We also introduced a viscous correction to the M1 radiative closure scheme which prevents artificial shocks of the radiation field near the rotation axis.

We performed a set of twelve axisymmetric, global simulations of optically thick accretion disks. From among them, seven

evolved into quasi-stationary, super-Eddington accretion disks, and the remaining five, corresponding to disks with the lowest, mostly sub-Eddington, accretion rates, collapsed because of runaway cooling.

Our study shows that:

(i) The proposed sub-grid dynamo prescription effectively prevents the poloidal magnetic field from decaying, and successfully drives the properties of the magnetic field towards the prescribed characteristics corresponding to the saturated state as inferred from 3D shearing sheet simulations. However, the agreement is not perfect inside the innermost stable orbit, where the radial velocities and magnetization are the largest.

(ii) The viscous correction to the M1 closure described in Appendix B successfully smooths the radiative field near the polar axis. Nevertheless, M1 closure still has its own limitations, and a more detailed study is required to assess how important the choice of closure scheme is for the dynamics of an accretion flow.

(iii) Optically thick accretion can take place in a quasi-stationary way for accretion rates $\dot{M} \gtrsim 2\dot{M}_{\text{Edd}}$. Simulations initiated with torii designed to provide lower accretion rates exhibited a run-away cooling leading to a disk collapse. The fact that the MRI seemed to be resolved before the collapse, and the critical accretion rate below which the collapse occurs ($\dot{M}_{\text{crit}} \approx 2\dot{M}_{\text{Edd}}$ which is where the transition between the middle, radiation pressure-dominated, and the top, advection-dominated, branches is expected) suggest that this is the result of a thermal instability. However, more detailed analysis is required to confirm this hypothesis. One should also keep in mind that although our dynamo-sustained magnetic field has similar properties to saturated fields obtained in 3D studies, our disks are turbulent only in the poloidal plane. Ultimately 3D simulations are needed for a self-consistent study of the onset of thermal instability.

(iv) The simulations of super-Eddington accretion flows we performed suggest that the radius outside which outflow in a wind is present ($R \approx 20$ and $R \approx 10$ for $a_* = 0$ and 0.9 , respectively) is smaller than for corresponding simulations of radiatively inefficient, optically thin disks (Narayan et al. 2012; Sądowski et al. 2013b). This fact suggest that winds are more effectively driven out in radiation-pressure supported optically thick disks. Within the range of accretion rates explored in our simulations with $a_* = 0$ ($2 \lesssim \dot{M}/\dot{M}_{\text{Edd}} \lesssim 500$) the relative power of the wind seems to be independent of the accretion rate. Extending this trend down would suggest that similar outflows may also occur in thin disks accreting at low rates and affect their dynamics.

(v) The total efficiency of super-critical accretion on a non-rotating BH is consistent among all four simulations we performed and corresponds to extraction of $\sim 4\%$ of the accreted rest mass energy, independent of the accretion rate. This is slightly less than the efficiency corresponding to a classical thin accretion disk around a non-rotating BH ($\eta_0 = 0.057$), but is much higher than the efficiencies predicted by the slim disk model (e.g., Sądowski 2011). This extra efficiency is related to the existence of outflows ejected by accretion. Because of limited duration and limited size of the simulation domain, we are not able to give exact radiative luminosities, and instead can only provide a lower limit (corresponding to the luminosity from inside the optically thin region of the domain). In most cases, this radiative luminosity estimate comprises only a small fraction of the total flux of outflowing energy.

(vi) Accretion disks around spinning BHs extract rotational energy from the BH, and this energy extraction process constitutes a large fraction of the total energy efficiency for the system. The energy extraction rate attributed to the Blandford-Znajek mecha-

nism has comparable efficiency to that measured in 3D simulations of optically thin advection dominated accretion flows (ADAFs). In this work, we are not able to study this in detail — axisymmetric simulations are limited to relatively weak magnetic fields at the BH, and thus we cannot resolve the magnetically arrested state (MAD).

(vii) The sub-grid dynamo model generates a turbulent field which overwrites the topology of the initial magnetic field (assuming weak starting fields). As a result, the magnetic field threading the horizon is not a simple dipole. It often changes polarity, and may have multipolar structure owing to the tangled nature of turbulent magnetic fields. Despite the complex multipolar nature of the magnetic field, the end result still seems to be efficient energy extraction from the BH at levels comparable to the prediction from the BZ mechanism. On average, the rapidly varying configuration has only slightly lower efficiency than a structured purely dipolar field.

(viii) Super-critical accretion is optically thick, and the photosphere may be located very close to the polar axis. For accretion rates exceeding $\sim 20\dot{M}_{\text{Edd}}$, there is no optically thin region at all inside $R = 5000$. In all cases, gas gradually rarifies, the funnel opens and photons diffuse into it from the optically thick region of outflowing gas.

(ix) The radiative luminosities in the funnel for the runs with a non-rotating BH are relatively low ($1.5 \div 2.1L_{\text{Edd}}$) despite significantly super-Eddington accretion rates. However, the corresponding radiative fluxes near the polar axis are extremely high, reaching ~ 1000 times the Eddington flux, $F_{\text{Edd}} = L_{\text{Edd}}/4\pi R^2$. It shows, that the radiative emission from a super-critical accretion disk is strongly collimated along the axis. If only a source with moderate accretion rate is observed down the funnel, the apparent luminosity of such a source will be orders of magnitude higher. To assess the relevance of this effect to the ultraluminous X-ray sources, detailed radiative transfer modeling is required.

5 ACKNOWLEDGEMENTS

AS and RN were supported in part by NSF grant AST1312651 and NASA grant NNX11AE16G. AT was supported by NASA through Einstein Postdoctoral Fellowship grant number PF3-140115 awarded by the Chandra X-ray Center, which is operated by the Smithsonian Astrophysical Observatory for NASA under contract NAS8-03060. We also acknowledge computational support from NSF via XSEDE resources (grant TG-AST080026N to RN and AS, and grant TG-AST100040 to AT), and from NASA (to RN and AS) via the High-End Computing (HEC) Program through the NASA Advanced Supercomputing (NAS) Division at Ames Research Center.

REFERENCES

- Abramowicz, M. A., Czerny, B., Lasota, J. P., & Szuszkiewicz, E. 1988, *Astrophysical Journal*, 332, 646
- Anninos, P., Fragile, P. C., & Salmonson, J. D. 2005, *Cosmos++: Relativistic Magnetohydrodynamics on Unstructured Grids with Local Adaptive Refinement*, *Astrophysical Journal*, 635, 723
- Blackman, E. G., Penna, R. F., & Varnière, P. 2008, *New Astronomy*, 13, 244
- Blaes, O., Hirose, S., & Krolik, J. H. 2007, *Astrophysical Journal*, 664, 1057
- Blaes, O., Krolik, J. H., Hirose, S., & Shabaltas, N. 2011, *Astrophysical Journal*, 733, 110

- Blandford, R. D., & Znajek, R. L. 1977, *Monthly Notices of the Royal Astronomical Society*, 179, 433
- Brandenburg, A., Nordlund, A., Stein, R. F., & Torkelsson, U. 1995, *Astrophysical Journal*, 446, 741
- Brandenburg, A. 2001, *Astrophysical Journal*, 550, 824
- Bucciantini, N., & Del Zanna, L. 2013, *Monthly Notices of the Royal Astronomical Society*, 428, 71
- Chandrasekhar, S. 1950, Oxford, Clarendon Press, 1950.,
- Cowling, T. G. 1933, *Monthly Notices of the Royal Astronomical Society*, 94, 39
- Del Zanna, L., Zanotti, O., Bucciantini, N., & Londrillo, P. 2007, *Astronomy & Astrophysics*, 473, 11
- De Villiers, J.-P., Hawley, J. F., & Krolik, J. H. 2003, *Astrophysical Journal*, 599, 1238
- Dubroca, B., & Feugeas, J. L. 1999, *CRAS*, 329, 915
- Duez, M. D., Liu, Y. T., Shapiro, S. L., & Stephens, B. C. 2004, *Physical Review D*, 69, 104030
- Gammie, C. F., McKinney, J. C., & Tóth, G. 2003, *Astrophysical Journal*, 589, 444
- Guan, X., Gammie, C. F., Simon, J. B., & Johnson, B. M. 2009, *Astrophysical Journal*, 694, 1010
- Hawley, J. F., Guan, X., & Krolik, J. H. 2011, *Astrophysical Journal*, 738, 84
- Hawley, J. F., Richers, S. A., Guan, X., & Krolik, J. H. 2013, *Astrophysical Journal*, 772, 102
- Hirose, S., Krolik, J. H. & Blaes, O. 2009a, *Astrophysical Journal*, 691, 16
- Hirose, S., Blaes, O., & Krolik, J. H. 2009b, *Astrophysical Journal*, 704, 781
- Jiang, Y.-F., Stone, J. M., & Davis, S. W. 2012, *Astrophysical Journal Suppl. Ser.*, 199, 14
- Jiang, Y.-F., Stone, J. M., & Davis, S. W. 2013, *Astrophysical Journal*, 778, 65
- Jiang, Y.-F., Stone, J. M., & Davis, S. W. 2014, arXiv:1403.6126
- Kawashima, T., Ohsuga, K., Mineshige, S., Heinzeller, D., Takabe, H., & Matsumoto, R. 2009, *Publications of the Astronomical Society of Japan*, 61, 769
- Komissarov, S. S. 1999, *Monthly Notices of the Royal Astronomical Society*, 303, 343
- Krolik, J. H., Hirose, S., & Blaes, O. 2007, *Astrophysical Journal*, 664, 1045
- Krolik, J. H., & Piran, T. 2012, *Astrophysical Journal*, 749, 92
- Landau, L. D., & Lifshitz, E. M. 1959, *Course of theoretical physics*, Oxford: Pergamon Press, 1959,
- Lasota, J.-P. 2001, *New Astronomy Reviews*, 45, 449
- Lasota, J.-P., Gourgoulhon, E., Abramowicz, M., Tchekhovskoy, A., & Narayan, R. 2014, *Physical Review D*, 89, 024041
- Levermore, C. D. 1984, *Journal of Quantitative Spectroscopy and Radiative Transfer*, 31, 149
- Li, L.-X., & Narayan, R. 2004, *Astrophysical Journal*, 601, 414
- McKinney, J. C. 2006, *Monthly Notices of the Royal Astronomical Society*, 368, 1561
- McKinney, J. C., Tchekhovskoy, A., & Blandford, R. D. 2012, *Monthly Notices of the Royal Astronomical Society*, 423, 3083
- McKinney, J. C., Narayan, R., Sądowski, A., & Tchekhovskoy, A. 2013, *Monthly Notices of the Royal Astronomical Society*, submitted
- Narayan, R., Sądowski, A., Penna, R. F., & Kulkarni, A. K. 2012, *Monthly Notices of the Royal Astronomical Society*, 426, 3241
- Ohsuga, K., Mineshige, S., Mori, M., & Yoshiaki, K. 2009, *Publications of the Astronomical Society of Japan*, 61, L7
- Ohsuga, K., & Mineshige, S. 2011, *Astrophysical Journal*, 736, 2
- Parker, E. N. 1955, *Astrophysical Journal*, 122, 293
- Penna, R. F., Kulkarni, A., & Narayan, R. 2013a, *Astronomy & Astrophysics*, 559, A116
- Penna, R. F., Sądowski, A., Kulkarni, A. K., & Narayan, R. 2013b, *Monthly Notices of the Royal Astronomical Society*, 428, 2255
- Penna, R. F., Narayan, R., & Sądowski, A. 2013c, *Monthly Notices of the Royal Astronomical Society*, 436, 3741
- Pozdnyakov, L. A., Sobol, I. M., & Syunyaev, R. A. 1983, *Astrophysics and Space Physics Reviews*, 2, 189
- Press, W. H., Flannery, B. P., & Teukolsky, S. A. 1986, Cambridge: University Press, 1986,
- Rybicki, G. B., & Lightman, A. P. 1979, New York, Wiley-Interscience, 1979. 393 p.,
- Sądowski, A. 2009, *Astrophysical Journal Suppl. Ser.*, 183, 171
- Sądowski, A. 2011, Ph.D. Thesis, Nicolaus Copernicus Astronomical Center, Polish Academy of Sciences, arXiv:1108.0396
- Sądowski, A., Narayan, R., Tchekhovskoy, A., & Zhu, Y. 2013a, *Monthly Notices of the Royal Astronomical Society*, 429, 3533
- Sądowski, A., Narayan, R., Penna, R., & Zhu, Y. 2013b, *Monthly Notices of the Royal Astronomical Society*, 436, 3856
- Sądowski, A., Narayan, R., McKinney, J. C., & Tchekhovskoy, A. 2014, *Monthly Notices of the Royal Astronomical Society*, 439, 503
- Shakura, N. I., & Sunyaev, R. A. 1973, *A&A*, 24, 337
- Skinner, M. A., & Ostriker, E. C. 2013, *Astrophysical Journal Suppl. Ser.*, 206, 21
- Sorathia, K. A., Reynolds, C. S., Stone, J. M., & Beckwith, K. 2012, *Astrophysical Journal*, 749, 189
- Tajima, Y., & Fukue, J. 1998, *Publications of the Astronomical Society of Japan*, 50, 483
- Tchekhovskoy, A., Narayan, R., and McKinney, J. C. 2010, *New Astron.*, 15, 749–754
- Tchekhovskoy, A., & McKinney, J. C. 2012, *Monthly Notices of the Royal Astronomical Society*, 423, L55
- Tóth, G. 2000, *Journal of Computational Physics*, 161, 605
- Turner, N. J., Stone, J. M., Krolik, J. H., & Sano, T. 2003, *Astrophysical Journal*, 593, 992
- Yuan, F. & Narayan, R. 2014, *Annual Reviews*, submitted

APPENDIX A: SUBGRID DYNAMO

We describe here the model we use to introduce an effective magnetic dynamo mechanism in an axisymmetric ideal MHD simulation. We start with the mean magnetic field evolution equation (Brandenburg 2001),

$$\frac{\partial \vec{B}}{\partial t} = \alpha \nabla \times \vec{B} + \eta \nabla^2 \vec{B}, \quad (\text{A1})$$

where α and η , are the dynamo and magnetic diffusivity coefficients, respectively. The first term on the left hand side describes the dynamo effect which generates poloidal magnetic field, and the second corresponds to the dissipation of the magnetic field. We treat the two components independently.

A1 α -effect

The magnetic field generation term may be written in the form,

$$\frac{\partial \vec{B}_p}{\partial t} = \alpha (\nabla \times \vec{B})_p, \quad (\text{A2})$$

where we restrict ourselves to the generation of orthonormal poloidal component \vec{B}_p . We expect field generation to happen on a dynamical timescale Ω_K^{-1} , therefore we introduce normalization factors,

$$\frac{1}{|\vec{B}_p|} \frac{\partial \vec{B}_p}{\partial t} = \alpha \frac{\Omega_K}{|J_p|} (\nabla \times \vec{B})_p, \quad (\text{A3})$$

where $J_p = (\nabla \times \vec{B})_p$ is the poloidal current, the magnitude of which we approximate as,

$$|J_p| = |(\nabla \times \vec{B})_p| \approx \frac{|B_\phi|}{H}, \quad (\text{A4})$$

with H being the disk scale height at the given radius.

The poloidal magnetic field may be expressed as,

$$\vec{B}_{\hat{p}} = (\nabla \times \vec{A})_{\hat{p}}, \quad (\text{A5})$$

where \vec{A} is the vector potential. Putting Eqs. A3, A4 and A5 together, we get,

$$\frac{\partial}{\partial t} (\nabla \times \vec{A})_{\hat{p}} = \Omega_K \alpha (\nabla \times \vec{B})_{\hat{p}} \frac{|\vec{B}_{\hat{p}}| H}{|B_{\hat{\phi}}|}. \quad (\text{A6})$$

Now we assume that all the terms outside the brackets are invariant with respect to curl, and get,

$$\frac{\partial A_{\hat{\phi}}}{\partial t} = \Omega_K \alpha B_{\hat{\phi}} \frac{|\vec{B}_{\hat{p}}| H}{|B_{\hat{\phi}}|}, \quad (\text{A7})$$

where we retain only the azimuthal components of the vector potential and magnetic field inside the curl since they are the source of the poloidal field.

Local 3D simulations of MHD turbulence, either in the shearing sheet approximation (e.g. Guan et al. 2009; Jiang, Stone, & Davis 2013), or global (Sorathia et al. 2012), have shown that the turbulent magnetic field saturates at a magnetic field angle,

$$\xi = \frac{b' b^\phi}{b^2} \approx \frac{|\vec{B}_{\hat{p}}|}{|B_{\hat{\phi}}|} = \xi_{\text{dyn}} \approx \frac{1}{4}. \quad (\text{A8})$$

We include this number into Eq. A7 and get,

$$\frac{\partial A_{\hat{\phi}}}{\partial t} = \alpha_{\text{dyn}} \Omega_K H B_{\hat{\phi}}, \quad (\text{A9})$$

where $\alpha_{\text{dyn}} = \alpha \xi_{\text{dyn}} \approx \alpha/4$. This is our basic dynamo prescription, except that we need some control factors.

We want to make sure that the dynamo does not generate too much poloidal magnetic field which would make the magnetic field angle exceed the expected value (Eq. A8). In three-dimensions, the dynamo is self-regulated, but it has to be limited manually in axisymmetry. We therefore introduce a factor,

$$f_{\xi} = \max \left(\frac{\xi_{\text{dyn}} - \xi}{\xi_{\text{dyn}}}, 0 \right), \quad (\text{A10})$$

which turns the dynamo off in regions that already have sufficient poloidal magnetic field.

The dynamo results partly from magnetic buoyancy which bends toroidal magnetic field lines and allows them to create poloidal field. Therefore, it is reasonable to assume that the dynamo effect is antisymmetric with respect to the equatorial plane. We impose this by introducing a factor,

$$f_{\text{eq}} = \frac{R}{H} \frac{\pi/2 - \theta}{\pi/2}, \quad (\text{A11})$$

where H and R are the local density scale height and radius, respectively, and θ is the polar coordinate.

The magnetic field saturates at the level discussed here only in the turbulent body of a disk. In the corona, the dynamo may not be as effective, and may lead to a completely different saturation state. Therefore we limit the sub-grid dynamo model to the interior of the disk, by introducing another scaling factor,

$$f_{\theta} = \max \left(1 - \left(\frac{\pi/2 - \theta}{\Theta_H} \right)^2, 0 \right), \quad (\text{A12})$$

where Θ_H is the polar angle corresponding to the density scale-height calculated after each time step according to Eq. 40.

Finally, we wish to eliminate the dynamo within the plunging

region where the flow is more laminar than turbulent. We achieve this through another factor,

$$f_R = \frac{1}{1 + \exp \left(-2.94 \frac{R - R_{\text{ISCO}}}{0.1 R_{\text{ISCO}}} \right)}, \quad (\text{A13})$$

which smoothly goes from $f_R = 1$ for $R \gg R_{\text{ISCO}}$ to $f_R = 0$ close to the BH horizon.

Applying the factors introduced above into Eq. A9 we get the ultimate formula for orthonormal coordinates,

$$\frac{\partial A_{\hat{\phi}}}{\partial t} = \alpha_{\text{dyn}} \Omega_K R B_{\hat{\phi}} f_R f_{\theta} f_{\xi} f_{\text{eq}}. \quad (\text{A14})$$

This can be generalized to non-orthonormal coordinates by,

$$\frac{\partial A_{\varphi}}{\partial t} = \alpha_{\text{dyn}} \Omega_K R g_{\phi\phi} B^{\varphi} f_R f_{\theta} f_{\xi} f_{\text{eq}}, \quad (\text{A15})$$

where for simplicity we considered only diagonal terms of the metric. The above formula is applied in a finite difference form (Eq. 32) after each time step to generate a dynamo-induced purely toroidal vector potential, which provides a weak correction to the poloidal magnetic field, which is then super-imposed on top of the preexisting field.

A2 Ω -effect

The mechanism described in the previous section constantly injects poloidal magnetic field in regions where the magnetic field angle (roughly equal to the ratio of poloidal to toroidal components) is too low. Radial magnetic field created this way is then sheared by the differential rotation creating extra toroidal component. In axisymmetry there is no mechanism to suppress this mechanism, and the gas quickly becomes over-magnetized. In 3D the magnetic pressure saturates roughly at 10% of the total pressure (Eq. 30, Blackman, Penna, & Varnière 2008; Hirose et al. 2009b; Jiang, Stone, & Davis 2013). To enforce this condition we damp the lab-frame toroidal component of the magnetic field on the dynamical timescale according to,

$$\frac{dB^{\varphi}}{dt} = -\alpha_{\text{damp}} \Omega_K B^{\varphi} f_R f_{\theta} f_{\beta'}, \quad (\text{A16})$$

where f_R (Eq. A13) and f_{θ} (Eq. A12) ensure that the damping occurs only outside the ISCO and within one scale-height, and the factor $f_{\beta'}$,

$$f_{\beta'} = \max \left(\frac{\beta' - \beta'_{\text{damp}}}{\beta'_{\text{damp}}}, 0 \right), \quad (\text{A17})$$

restricts the damping to over-magnetized regions ($\beta' > \beta'_{\text{damp}} = 0.1$).

A3 Validation

To evaluate the effectiveness of the sub-grid dynamo model, and to compare it with 3D simulations, we performed a test non-radiative, global, GRMHD simulation set up in a similar way to the $a_* = 0.0$ SANE model from Narayan et al. (2012). We used exactly the same initial torus as in the reference 3D simulation. We threaded the torus with multiple quadrupolar loops of a weak magnetic field, resembling the initial state for the corresponding radiative runs discussed in the main part of the paper. We used a grid of 256x256 points with cells spaced logarithmically in radius and uniformly in polar angle. The adopted vertical resolution was a factor of two higher than in Narayan et al. (2012), because the reference 3D run was only

marginally resolved. We adopted the same dynamo parameters as for the radiative runs, i.e., $\alpha_{\text{dyn}} = 0.05$, $\xi_{\text{dyn}} = 0.25$, $\alpha_{\text{damp}} = 1.0$ and $\beta'_{\text{damp}} = 0.1$.

Figure A1 shows the dynamo-generated correction to the poloidal magnetic field at early (top), and late (bottom panel) times in the simulation. At $t = 100$ (top panel), the MRI has not yet developed and the poloidal magnetic field (right panel) follows the initial configuration. However, although initially there was no azimuthal magnetic field, differential rotation quickly stretches the radial component and generates toroidal field, B^ϕ , which triggers the dynamo action. The left panel shows the dynamo correction (contour levels are arbitrary) which was obtained by taking the curl of the dynamo-generated vector potential A_ϕ (Eq. A15) which follows $\propto RB^\phi$. One may expect flipping polarity of the resulting dynamo field where this quantity changes sign. This is indeed the case, as the dashed contours in the left panel of Figure A1 show. A similar flip takes place at the equatorial plane because of the assumed antisymmetry (Eq. A11). The vertical extent of the region affected by the dynamo is limited by the density scaleheight through Eq. A12.

The bottom panel of Figure A1 shows an advanced stage of the test simulation ($t = 100,000$). The MRI-driven turbulence is still evident despite the very late time (for comparison turbulence in the same disk evolved without the sub-grid dynamo decays after $t \approx 5,000$). Turbulent disk structure implies turbulent distribution of B^ϕ which results in more chaotic dynamo contribution, as seen in the left panel. Once again, the poloidal loops flip signs where $RB^\phi = 0$ (dashed contours), and at the equatorial plane.

To obtain the mean properties of the magnetic field, we averaged the disk solution over time $t = 50,000 \div 100,000$. In Figure A2 we plot the magnetic field angle ξ (solid lines), and the magnetic to total pressure ratio β' (dashed lines) for our test simulation, and, for comparison, for the 3D reference run. In the test simulation, the magnetic field angle settled down on the prescribed value $\xi_{\text{dyn}} = 0.25$ for the whole converged region ($R \lesssim 75$) outside the marginally stable orbit. The magnetic field angle inside the ISCO, where the dynamo model is not applied (Eq. A13), departs from $\xi_{\text{dyn}} = 0.25$ and increases, although non-monotonically, towards the horizon. The mean magnetic field angle obtained in the 3D simulation is closer to 0.2 and smoothly increases towards the horizon. The two profiles are in qualitative agreement. We suspect that the 3D run gave an angle of 0.2 rather than the more accurate value of 0.25 (Sorathia et al. 2012), because of insufficient resolution.

The magnetic to total pressure ratio in our test axisymmetric simulation is close to the prescribed value $\beta'_{\text{damp}} = 0.1$ near the radius of convergence ($R \approx 75$) and slowly increases inward, reaching $\beta' \approx 0.3$ at the ISCO. Inside that critical radius, it grows rapidly towards the horizon as the gas in the plunging region is highly magnetized. The departure of the pressure ratio from the target value $\beta'_{\text{damp}} = 0.1$ results from the fact that the radial velocity in a radiatively inefficient flow is large enough not to give the damping prescription (Eq. A16) enough time to balance the shearing-induced generation of the toroidal magnetic field. A similar increase in magnetization is clear also in the 3D run. However, the value of the pressure ratio in the 3D simulation was significantly lower ($\beta' = 0.02$ for $R \gtrsim 30$), is inconsistent with results from local shearing sheet studies (e.g., Blackman, Penna, & Varnière 2008; Jiang, Stone, & Davis 2013). Once again, we suspect this is a result of inadequate resolution.

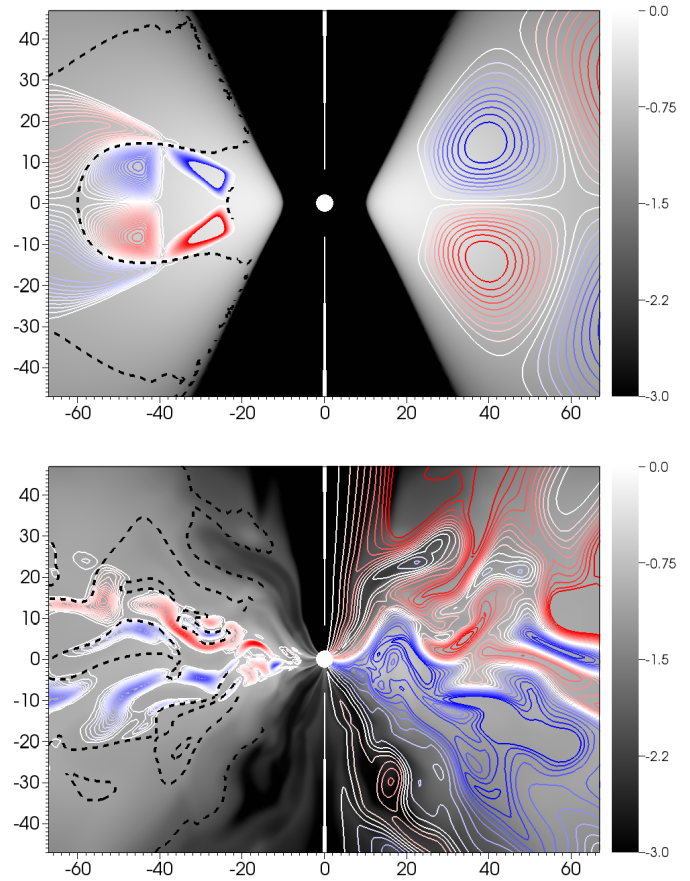


Figure A1. Snapshots of the test, non-radiative GRMHD simulations, showing the poloidal magnetic field (right) and the dynamo-generated correction (left panel). Contours show the magnetic field lines. Red and blue correspond to clockwise and counter-clockwise loops, respectively. Grey colors show the logarithm of density. The top and bottom panels corresponds to an early stage of the simulation ($t = 100$), and a late one ($t = 100,000$), respectively. The dashed contour in the left panels shows where RB^ϕ changes sign.

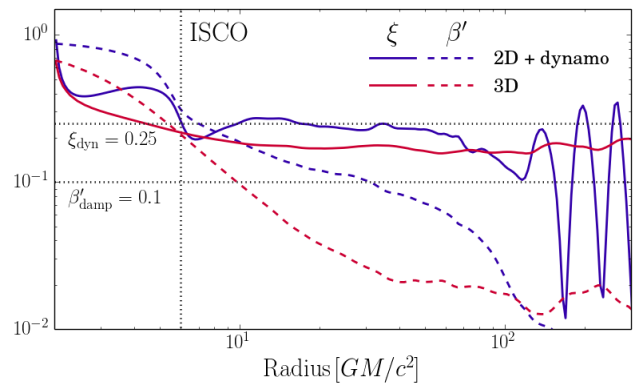


Figure A2. Magnetic field angle ξ (Eq. 29, solid lines), and magnetic to total pressure ratio β' (dashed lines) for a test axisymmetric GRMHD run with dynamo (blue lines), and a full 3D simulation (Narayan et al. 2012, red lines). The horizontal dotted lines show the target values of ξ and β' used by the sub-grid dynamo model. The vertical line denotes the radius of the ISCO.

APPENDIX B: RADIATIVE VISCOSITY FOR M1 CLOSURE

The radiative closure scheme adopted in this work, the M1 closure, limits the set of possible angular distributions of the radiation. M1 assumes that the specific intensity in the lab frame can be obtained by boosting an isotropic distribution. This is a strong assumption and, obviously, often will not be satisfied. The simplest case in which M1 closure fails, is a problem consisting of two discrete, isotropic sources of light, emitting into an optically thin medium. M1 closure allows for specific intensities boosted only along one direction – the direction of the net flux (while the photons want to cross each other and propagate in two distinct directions). The result is that M1 causes an unphysical pile up of photons where the two beams cross.

Fortunately, accretion disks almost never have distinct point sources of radiation where the radiation field can clash with other point sources. Photons are generated at the photosphere, which is a continuous extended source (though it may be turbulent and clumpy). Therefore, M1 closure is expected to work reasonably well for disks.

However, M1 closure has another flaw which may be important for BH accretion disks. As discussed in the Appendix of Sądowski et al. (2013a), photons emitted from rotating disk, when approaching the polar axis, mix in a way that overestimates their angular momentum and prevents radiation from reaching the axis, creating a shock-like discontinuity in the radiative field just off the axis. In simulations, this feature appears intermittently due to the turbulent nature of the accretion flow, and is more pronounced for thin disks.

In this paper we overcome⁵ this flaw by introducing an artificial viscosity in the radiation field which diffuses the shock and drives the radiation field towards a more realistic distribution.

In hydrodynamics, the viscous contribution to the gas stress-energy tensor is often calculated as the product of a dynamic viscosity coefficient and the shear tensor which describes the rate of shear of fluid velocities (Landau & Lifshitz 1959). In the covariant formulation of the M1 closure used in this paper, the radiation field is described using the velocity of the radiation rest frame, u_R^μ and its energy density in that frame, E_R . The correspondence between the description of the gas and radiation, makes it possible to apply a similar formalism for viscosity in context of the radiation field by using the radiative rest frame velocities to calculate the (radiative) shear tensor, and to use the radiative energy density to calculate the corresponding viscosity coefficient.

We therefore introduce a viscous correction to the radiative stress energy tensor,

$$R_{\text{visc}}^{\mu\nu} = -2\nu E_R \sigma^{\mu\nu} \quad (\text{B1})$$

where ν is the viscosity coefficient (defined below), E_R is the radiative energy density in the radiation rest frame, and $\sigma^{\mu\nu}$ is the shear tensor, calculated from the radiation rest frames velocity field u_R^μ , through,

$$\sigma^{\mu\nu} = \frac{1}{2} \left(u_{R;\alpha}^\mu P^{\alpha\nu} + u_{R;\alpha}^\nu P^{\alpha\mu} \right) - \frac{1}{3} P^{\mu\nu}, \quad (\text{B2})$$

where $P^{\alpha\beta} = g^{\alpha\beta} + u_R^\alpha u_R^\beta$ is the projection tensor. The derivatives are calculated using radiative velocities from the previous time step,

⁵ To rephrase Polish journalist Stefan Kisielewski commenting on socialism: “M1 closure heroically overcomes difficulties unknown to any other closure”.

and the time derivatives are set to zero for stability (compare Duez et al. 2004). The viscous coefficient ν is set to some fraction (α_{rv}) of the mean free path of photons, λ ,

$$\nu = \alpha_{\text{rv}} \lambda, \quad (\text{B3})$$

where we estimate the mean free path as the inverse of the mean opacities, but limited in the optically thin limit to the local radial coordinate R ,

$$\lambda = \min \left(R, \frac{1}{\rho(\kappa_a + \kappa_{\text{es}})} \right). \quad (\text{B4})$$

The radiative viscosity is suppressed in optically thick regions because λ becomes very small.

The viscous correction to the radiative stress-energy tensor (Eq. B1) is applied only when calculating fluxes at the cell faces (Eq. 9). Because we do not modify the algorithm, and apply the advective operator explicitly, we need to make sure that the viscous correction does not violate the usual Courant stability criterion (Press et al. 1986). For this purpose, we limit ν (Eq. B3) with,

$$\nu_{\text{lim}} = \frac{\Delta x_{\text{min}}}{2\Delta t}, \quad (\text{B5})$$

where Δx_{min} is the length of the shortest cell edge, and Δt is the timestep.

The magnitude of the radiative viscosity is controlled by the parameter α_{rv} . To choose the right value we compare the synthetic radiation field generated by a radiating slab resembling a thin accretion disk, with the analytical solution obtained in the Newtonian approximation following Tajima & Fukue (1998). The latter is given by,

$$\epsilon(R, z) \propto \int_0^\infty \int_0^{2\pi} \left(1 - \sqrt{\frac{6}{R_d}} \right) R_d^{-3} \frac{I_{\text{M1}}(\mu)}{(1 + z_{\text{Dop}})^4} d\Omega, \quad (\text{B6})$$

where R_d is the radius at the equatorial plane, $I_{\text{M1}}(\mu)$ is the angular distribution of photons at the disk plane with respect to angle μ , z_{Dop} is the Doppler factor due to the orbital motion in the disk plane, $v^\varphi = R^{-1/2}$, and $d\Omega$ is an element of solid angle.

We set up a corresponding problem in KORAL on a grid in spherical coordinates (no BH in the center), with radial coordinate spaced logarithmically. The opacities were set to zero, the radiative energy density at the lower, emitting boundary was set to,

$$\hat{E} \propto \left(1 - \sqrt{\frac{6}{R}} \right) R^{-3}, \quad (\text{B7})$$

for $R > 6$, and the orthonormal radiative flux in the comoving frame was set to,

$$F^\theta = -0.5\hat{E}, \quad (\text{B8})$$

as appropriate for radiation escaping from optically thick slab. The corresponding specific intensity in the lab frame may be obtained by boosting the isotropic distribution with radiation rest frame velocity $\beta \approx 0.394$, to get (Rybicki & Lightman 1979),

$$I_{\text{M1}}(\mu, \beta) \propto \frac{(1 - \beta^2)^2}{(1 - \beta\mu)^4}, \quad (\text{B9})$$

which describes the effective limb darkening of radiation from disk surface, and is used in Eq. B6. This form of limb darkening is implied by the intrinsic M1 assumption about the form of specific intensities, and, by accident, matches quite well with limb darkening induced from vertical structure of emitting disk (Chandrasekhar 1950).

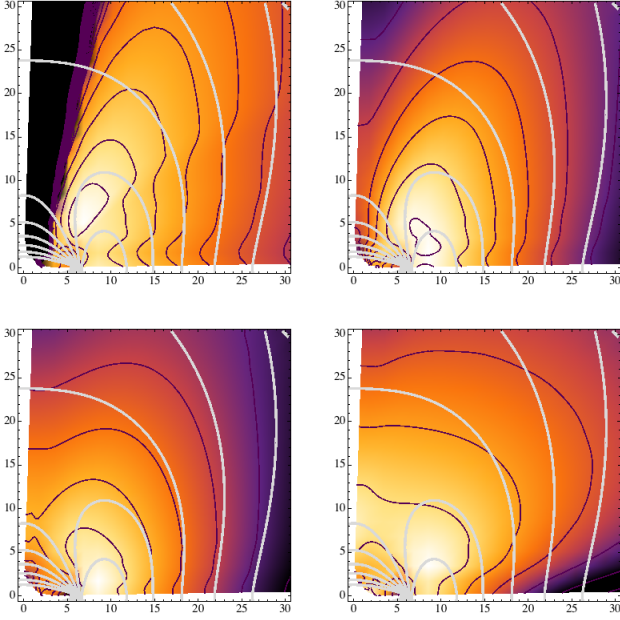


Figure B1. Comparison of the analytical radiation field (Eq. B6, light gray contours) with the numerical one (colors and dark contours) calculated using the M1 scheme and the radiative viscosity with $\alpha_{rv} = 0.0, 0.05$ (top panels, left to right), 0.1 , and 0.5 (bottom panels).

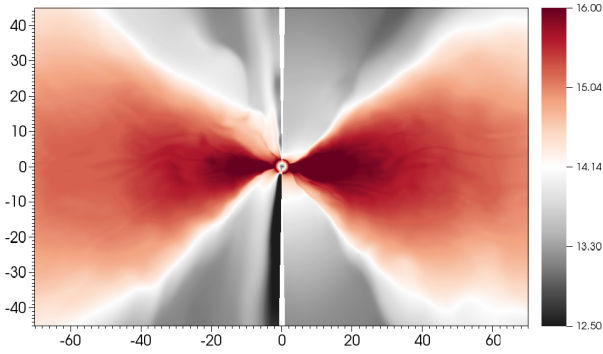


Figure B2. Comparison of the radiative energy distribution for runs without (left) and with (right panel, **r300a0**) radiative viscosity at $t = 65,000$.

Figure B1 compares the analytical and numerical solutions. White contours show the radiative energy distribution obtained from Eq. B6. Colors and black contours show the numerical solution obtained with KORAL for $\alpha_{rv} = 0$ (first panel, no viscosity), 0.05 , 0.1 , and 0.5 (lower right panel). The numerical solution with no viscosity exhibits an unphysical funnel near the axis that is devoid of radiation. This feature disappears once radiative viscosity is included. Out of the three values of α_{rv} considered, $\alpha_{rv} = 0.1$ provides the best match to the analytical solution, and is the value adopted in the simulations described in the main part of this paper. Figure B2 shows a snapshot of the **r300a0** simulation at $t = 65,000$ (right), and a corresponding snapshot from an otherwise identical simulation, but with no radiative viscosity (left panel). The latter clearly shows an empty, unphysical funnel near the axis (especially in the lower half). The empty region appears intermittently.